



HAL
open science

Crystal structures and local environments of NASICON-type $\text{Na}_3\text{FeV}(\text{PO}_4)_3$ and $\text{Na}_4\text{FeV}(\text{PO}_4)_3$ positive electrode materials for Na-ion batteries

Sunkyu Park, Jean-Noël Chotard, Dany Carlier, Iona Moog, Matthieu Courty,
Mathieu Duttine, François Fauth, Antonella Iadecola, Laurence Croguennec,
Christian Masquelier

► To cite this version:

Sunkyu Park, Jean-Noël Chotard, Dany Carlier, Iona Moog, Matthieu Courty, et al.. Crystal structures and local environments of NASICON-type $\text{Na}_3\text{FeV}(\text{PO}_4)_3$ and $\text{Na}_4\text{FeV}(\text{PO}_4)_3$ positive electrode materials for Na-ion batteries. *Chemistry of Materials*, 2021, 33 (13), pp.5355-5367. 10.1021/acs.chemmater.1c01457 . hal-03350982

HAL Id: hal-03350982

<https://hal.science/hal-03350982>

Submitted on 21 Sep 2021

HAL is a multi-disciplinary open access archive for the deposit and dissemination of scientific research documents, whether they are published or not. The documents may come from teaching and research institutions in France or abroad, or from public or private research centers.

L'archive ouverte pluridisciplinaire **HAL**, est destinée au dépôt et à la diffusion de documents scientifiques de niveau recherche, publiés ou non, émanant des établissements d'enseignement et de recherche français ou étrangers, des laboratoires publics ou privés.

Crystal Structures and Local Environments of NASICON-type $\text{Na}_3\text{FeV}(\text{PO}_4)_3$ and $\text{Na}_4\text{FeV}(\text{PO}_4)_3$ Positive Electrode Materials for Na-ion Batteries

Sunkyu Park ^{1,2,3}, Jean-Noël Chotard ^{1,5}, Dany Carlier ^{2,5}, Iona Moog ³, Matthieu Courty ¹,
Mathieu Duttine ², François Fauth ⁴, Antonella Iadecola ⁵, Laurence Croguennec ^{*,2,5} and
Christian Masquelier ^{*,1,5}

¹ *Laboratoire de Réactivité et de Chimie des Solides, Université de Picardie Jules Verne,
CNRS-UMR 7314, F-80039 Amiens Cedex 1, France*

² *CNRS, Univ. Bordeaux, Bordeaux INP, ICMCB UMR 5026, F-33600 Pessac, France*

³ *TIAMAT, 15 Rue Baudelocque, 80000 Amiens*

⁴ *CELLS-ALBA Synchrotron, Cerdanyola del Vallès, E-08290 Barcelona, Spain*

⁵ *RS2E, Réseau Français sur le Stockage Electrochimique de l'Energie, FR CNRS 3459,
F-80039 Amiens Cedex 1, France*

* corresponding authors at christian.masquelier@u-picardie.fr and Laurence.Croguennec@icmcb.cnrs.fr

Abstract

In this work, we investigate the crystal chemistry of Fe/V-mixed NASICON $\text{Na}_3\text{FeV}(\text{PO}_4)_3$ and $\text{Na}_4\text{FeV}(\text{PO}_4)_3$ compositions structurally related to $\text{Na}_3\text{V}_2(\text{PO}_4)_3$, a positive electrode for Na-ion batteries. To synthesize $\text{Na}_4\text{FeV}(\text{PO}_4)_3$, various synthesis routes (solid-state, sol-gel assisted, and electrochemical syntheses) were investigated. Direct syntheses resulted in forming a NASICON-type phase with the presence of NaFePO_4 and Na_3PO_4 impurities. The successful preparation of pure $\text{Na}_4\text{FeV}(\text{PO}_4)_3$ has been achieved by electrochemical sodiation of $\text{Na}_3\text{FeV}(\text{PO}_4)_3$. Both synchrotron X-ray absorption and Mössbauer spectroscopies allowed probing the local V and Fe environments and their oxidation states in $\text{Na}_3\text{FeV}(\text{PO}_4)_3$ and $\text{Na}_4\text{FeV}(\text{PO}_4)_3$. $\text{Na}_3\text{FeV}(\text{PO}_4)_3$ crystallizes in the space group $C2/c$ ($a = 15.1394(2)$ Å; $b = 8.72550(12)$ Å; $c = 21.6142(3)$ Å; $\beta = 90.1744(9)^\circ$, and $Z = 12$), and it is isostructural to an ordered α -form of $\text{Na}_3\text{M}_2(\text{PO}_4)_3$ ($M = \text{Fe}, \text{V}$). It presents a superstructure due to Na^+ ordering, as confirmed with differential scanning calorimetry and *in situ* temperature X-ray diffraction. The electrochemically-sodiated $\text{Na}_4\text{FeV}(\text{PO}_4)_3$ powder crystallizes in the space group $R-3c$ ($a = 8.94656(8)$ Å, $c = 21.3054(3)$ Å, and $Z = 6$) within which the two sodium sites, Na(1) and Na(2), are almost fully occupied. $\text{Na}_4\text{FeV}(\text{PO}_4)_3$ allows the electrochemical extraction of 2.76 Na^+ per formula unit within the voltage range of 1.3 – 4.3 V vs. Na^+/Na through the $\text{Fe}^{\text{III/II}}$, $\text{V}^{\text{IV/III}}$, and $\text{V}^{\text{V/IV}}$ redox couples. This identifies an interesting material for Na-ion batteries.

Introduction

NASICON-type $\text{Na}_3\text{V}_2(\text{PO}_4)_3$ is one of the most exploited positive electrode materials for Na-ion batteries due to its robust crystal structure, providing long cycle life and great rate capability.¹⁻⁷ The three-dimensional NASICON structure of general formula $\text{A}_x\text{MM}'(\text{XO}_4)_3$ is composed of lantern units stacked along the $[001]_{\text{hexagonal}}$ direction and made of two MO_6 and $\text{M}'\text{O}_6$ octahedra, not connected between each other but sharing corners with three XO_4 tetrahedra. This framework generates two interstitial sites, M(1) and M(2), generally occupied by alkaline ions. When A is Na^+ , one Na^+ ion can occupy the M(1) and the M(2) site up to three Na^+ ions, per formula unit. These interstitial sites are connected with three-dimensional conduction pathways allowing fast (de)intercalation of Na^+ ions without a collapse of the host structure.⁸

The crystal structure of $\text{Na}_3\text{V}_2(\text{PO}_4)_3$ has been recently revisited, clearly demonstrating that it cannot be described with the typical space group $R-3c$ model at room temperature, but with a monoclinic unit cell taking into account the ordering of Na^+ ions and vacancies within the $\text{V}_2(\text{PO}_4)_3$ framework.⁹ In fact, three reversible structural transitions have been identified using differential scanning calorimetry (DSC): $\alpha \leftrightarrow \beta$ at 26 °C, $\beta \leftrightarrow \beta'$ at 119 °C and $\beta' \leftrightarrow \gamma$ at 177 °C, with subtle modifications in the Na^+ sites' occupancies. The low-temperature form α ($C2/c$, $Z = 12$) is characterized by a superstructure due to long-range Na^+ ordering. The two intermediate-temperature β and β' monoclinic phases are incommensurate modulated structures. The rhombohedral form γ ($R-3c$, $Z = 6$) appears only above 180 °C, in which the Na atoms are fully disordered on the M(1) and M(2) sites. Similarly, two phase transitions ($\alpha \leftrightarrow \beta$ at 95 °C and $\beta \leftrightarrow \gamma$ at 145 °C upon heating) were also observed for the pure iron counterpart $\text{Na}_3\text{Fe}_2(\text{PO}_4)_3$.¹⁰⁻¹³

When used as a positive electrode for Na-ion batteries, $\text{Na}_3\text{V}_2(\text{PO}_4)_3$ allows the extraction/insertion of only two Na^+ per formula unit leading to a moderate specific capacity of 118 mAh/g even though it still possesses high power capabilities.¹⁻⁷ Improving the specific capacity while keeping the solid NASICON framework structure is an important challenge,

thus several strategies were proposed.^{1,2,14-18} An obvious one would be to extract the third Na^+ from $\text{Na}_3\text{V}_2(\text{PO}_4)_3$ through the activation of the $\text{V}^{\text{V}}/\text{V}^{\text{IV}}$ redox couple, but this has been reported to be thermodynamically and kinetically unfavorable.^{14,15} Another strategy is to tune the polyanionic framework by partially replacing the phosphate groups (PO_4^{3-}) by silicate groups (SiO_4^{4-}) so to prepare the Na-rich $\text{Na}_{3+x}\text{V}_2(\text{PO}_4)_{3-x}(\text{SiO}_4)_x$ solid solution. Such compositions, with $x = 0.1, 0.2$ and 0.4 , were recently reported for the first time, but without evidence of extra capacity probably since high voltage domain has not been explored.¹⁶ Electrochemical pre-sodiation of $\text{Na}_3\text{V}_2(\text{PO}_4)_3$ to yield $\text{Na}_4\text{V}_2(\text{PO}_4)_3$ was also proposed, either to compensate for the irreversible capacity loss observed during the first cycle in full cell¹⁷, or to increase the energy density of $\text{Na}_3\text{V}_2(\text{PO}_4)_3 \parallel \text{Na}_3\text{V}_2(\text{PO}_4)_3$ symmetric cells.¹⁸

Alternatively, various substitutions on the transition metal site were studied. Thanks to the excellent tunability of the NASICON structure, many different compositions could be explored, exemplified by $\text{Na}_x(\text{M},\text{M}')_2(\text{PO}_4)_3$ with $\text{M},\text{M}' = \text{Al},^{19} \text{Ti},^{20-25} \text{V},^{4-7,14-18,21} \text{Cr},^{22,24,26,27} \text{Mn},^{23,28-33} \text{Fe},^{24,28,30,34-37} \text{Nb},^{25} \text{Zr}^{29}$. However, most of the materials have shown no meaningful capacity increase when the electrochemical reaction was limited to the exchange of two Na^+ ions. Recently, several Na-rich compounds $\text{Na}_{3+x}\text{MM}'(\text{PO}_4)_3$ ($\text{MM}' = \text{MnV},^{31,32} \text{MnCr},^{33} \text{FeV},^{34-36} \text{MgV}^{38}$) have been reported as attempts to reach higher specific capacities through the possible extraction of more than two Na^+ per formula unit. The main criteria to design such compounds would be (i) the substitution by electrochemically active divalent elements such as Mn^{II} and Fe^{II} and (ii) the activation of multi-electron redox reactions on at least one of the transition metals. For instance, $\text{Na}_4\text{Mn}^{\text{II}}\text{V}^{\text{III}}(\text{PO}_4)_3$ ^{31,32} and $\text{Na}_4\text{Mn}^{\text{II}}\text{Cr}^{\text{III}}(\text{PO}_4)_3$ ³³ fulfil these two conditions and thus show the possible extraction of three Na^+ ions during the first charge, but drastic capacity fading was rapidly observed due to irreversible structural modifications occurring at high voltage.^{31,32} On the contrary, despite the multi-electron redox reaction involving the V^{III} cation, $\text{Na}_{3.7}\text{Mg}_{0.7}\text{V}^{\text{III}}_{1.3}(\text{PO}_4)_3$ is less attractive since Mg^{II} is not electrochemically active.³⁸ Only few Na-rich $\text{Na}_4\text{MM}'(\text{PO}_4)_3$ compositions have been explored so far among the high number of possible compositions predicted by first-principles calculations.³⁹

Remarkably, $\text{Na}_4\text{Fe}^{\text{II}}\text{V}^{\text{III}}(\text{PO}_4)_3$ has not been reported yet in the literature although there have been attempts to prepare it.^{30,34,35} De Boisse et al. reported a systematic study of $\text{Na}_{3+x}\text{Fe}^{\text{II}}\text{V}^{\text{III}}_{2-x}(\text{PO}_4)_3$ ($0 \leq x \leq 1$ with 0.1 increment) using solid-state synthesis, showing that secondary phases (mainly NaFePO_4) appeared for $x > 0.5$.³⁴ Hadouchi et al. also attempted to synthesize $\text{Na}_4\text{Fe}^{\text{II}}\text{V}^{\text{III}}(\text{PO}_4)_3$, but obtained a sodium-deficient composition $\text{Na}_{3.41}\square_{0.59}\text{FeV}(\text{PO}_4)_3$ with mixed valence $\text{Fe}^{\text{II}}/\text{Fe}^{\text{III}}$.³⁵ $\text{Na}_4\text{FeV}(\text{PO}_4)_3$ is particularly interesting since it could be more cost-effective than $\text{Na}_3\text{V}_2(\text{PO}_4)_3$ and three Na^+ exchange is principally feasible through the successive activations of the $\text{Fe}^{\text{III/II}}$, $\text{V}^{\text{IV/III}}$, and $\text{V}^{\text{V/IV}}$ redox couples.

In this study, we present the synthesis conditions of our various attempts to obtain the stoichiometric composition $\text{Na}_4\text{Fe}^{\text{II}}\text{V}^{\text{III}}(\text{PO}_4)_3$ as a pure phase. It was difficult to prepare a phase-pure $\text{Na}_4\text{Fe}^{\text{II}}\text{V}^{\text{III}}(\text{PO}_4)_3$ powder as many secondary phases appeared for the samples synthesized through direct syntheses. On the other hand, electrochemical synthesis using $\text{Na}_3\text{Fe}^{\text{III}}\text{V}^{\text{III}}(\text{PO}_4)_3$ as a precursor gave a pure $\text{Na}_4\text{Fe}^{\text{II}}\text{V}^{\text{III}}(\text{PO}_4)_3$ phase. To further study the crystal chemistry of both compositions (Na_3 and Na_4), and to study local environments and valence states of iron and vanadium, Mössbauer and synchrotron X-ray absorption spectroscopies were performed. During structural determinations of both compositions, an ordered superstructure was observed for $\text{Na}_3\text{FeV}(\text{PO}_4)_3$ at 298 K, confirmed with Differential Scanning Calorimetry (DSC) and *in situ* temperature XRD. We propose a new structural model for $\text{Na}_3\text{FeV}(\text{PO}_4)_3$, which can explain all the superstructure diffraction peaks, thanks to the analysis of high-angular resolution synchrotron X-ray diffraction data. The crystal structure of the fully-sodiated, electrochemically-active, $\text{Na}_4\text{FeV}(\text{PO}_4)_3$ composition is reported for the first time and discussed in details.

Experimental

Preparation of $\text{Na}_4\text{FeV}(\text{PO}_4)_3$ through direct syntheses. $\text{Na}_4\text{FeV}(\text{PO}_4)_3$ was prepared by solid-state and sol-gel methods. The solid-state method used stoichiometric amounts of Na_3PO_4 (Acros organics, 96 %), NaPO_3 , $\text{FeC}_2\text{O}_4 \cdot 2\text{H}_2\text{O}$ (Alfa Aesar, 99 %), and home-made VPO_4 in a molar ratio of 1:1:1:1. NaPO_3 was prepared from NaH_2PO_4 (Sigma-Aldrich, 99 %) under

vacuum drying at 250 °C overnight and then stored under Ar. VPO₄ was prepared as described in details elsewhere.³¹ The stoichiometric powder mixture was first ball-milled in a planetary mill for 12 h (10 minutes run followed by 10 minutes rest) at 400 rpm in Argon, the atmosphere used for the subsequent steps to avoid oxidation of Fe^{II}. The resulting powder was then pre-heated at 400 °C for 4 h (under Ar) and then mixed again in a mortar and pelletized prior to annealing at 700 °C for 20 h (under Ar). The sol-gel method used a solution of Fe(C₂H₃O₂)₂ (Sigma-Aldrich, 95 %), C₁₀H₁₄O₅V (Sigma-Aldrich, 97 %), citric acid (Alfa Aesar, 99 %) and oxalic acid (Sigma-Aldrich, 98 %), in a molar ratio of 1:1:2:1 and mixed in deionized (DI) water and ethanol (50/50 by volume) using a magnetic stirrer. Then a solution of CH₃COONa (Prolabo, 99 %) and NH₄H₂PO₄ (Sigma-Aldrich, 98.5 %) in deionized water in a molar ratio of 4:3 was added dropwise into the former solution. The solution thus obtained was dried overnight at 80°C in an oil bath under continuous stirring before being placed in an oven. The obtained powder was ground and pre-heated at 400 °C for 4 h in Ar. The resulting powder was then mixed in a mortar and annealed at 700°C for 10 h under either Ar or Ar/H₂ (95/5) atmosphere.

Preparation of Na₃FeV(PO₄)₃ through electrochemical sodiation. Na₃FeV(PO₄)₃ was prepared by a simple straightforward solid-state method. Stoichiometric amounts of Na₃PO₄ (Acros organics, 96 %), FePO₄•2H₂O (Sigma-Aldrich) and synthesized VPO₄ in a molar ratio of 1:1:1 were ball-milled in a SPEX 8000 mixer for 1 h. The resulting powder was heated at 400 °C for 4 h in Ar and then at 800 °C for 10 h in Ar with an intermediate regrinding. Then, composite electrodes were prepared by mixing the Na₃FeV(PO₄)₃ powder and carbon black (Alfa Aesar, 99.9+%) (80/20 in wt%) before being dried overnight at 80 °C under vacuum. These electrodes were assembled as working electrodes versus Na metal as reference electrode in CR2032-type coin cells in an Ar-filled glove box. One sheet of Celgard and glass fiber were used as separators and the electrolyte was composed of 1 M NaPF₆ (Strem Chemicals; 99%) in EC/DMC (1:1 mass ratio) with 2 wt.% of FEC. A slow electrochemical reaction rate of C/20 (1 C = 58.2 mA/g, or 20 h for the exchange of 1Na⁺ / 1e⁻) was used to intercalate Na⁺ into Na₃FeV(PO₄)₃, with a cut-off voltage of either 2.0 or 1.3 V versus Na⁺/Na.

Laboratory X-ray diffraction (XRD) was performed in Debye–Scherrer geometry on a PANalytical Empyrean diffractometer using $\text{Cu}_{\text{K}\alpha_{1,2}}$ radiation with powder in 0.3-mm diameter capillary. Synchrotron X-ray diffraction (SXR) measurements were conducted at room temperature on the MSPD beamline of the ALBA synchrotron in Spain.⁴⁰ Data were collected in Debye-Scherrer geometry, at a wavelength of 0.8266 Å, still using a 0.3 mm diameter capillary. The position sensitive detector, MYTHEN detector, was used to rapidly collect pattern in the 2θ angular range of 2 - 60°, with a 2θ step size of 0.006°. *In situ* temperature-controlled X-ray diffraction measurements were performed using an Anton Paar HTK1200 furnace on a PANalytical X'Pert Pro diffractometer, at the $\text{Co}_{\text{K}\alpha_{1,2}}$ radiation. XRD patterns collected with every 10 °C from room temperature up to 150 °C and then cooling down to 30 °C with one hour of acquisition for each pattern. To stabilize temperature, the heating rate was 1 °C/min and being held for 10 min at each temperature before the pattern's acquisition. Diffraction data analysis was performed using the FullProf Suite⁴¹ and JANA2006⁴².

⁵⁷Fe Mössbauer measurements were performed using a constant acceleration Halder-type spectrometer operating in transmission geometry with ⁵⁷Co source (embedded in Rh matrix) at room temperature. The velocity scale was calibrated using the characteristic sextet of a pure $\alpha\text{-Fe}^0$ foil as reference. Mössbauer hyperfine parameters were refined with the WinNormos software (Wissenschaftliche Elektronik GmbH). It is important to mention that various components of a Mössbauer spectrum may have different values of Lamb-Mössbauer factor (f). This parameter, also known as the recoil-free fraction, strongly affects the intensity of the Mössbauer effect and thus the absorption area of the observed signal. At room temperature, significant difference in Lamb-Mössbauer factors can lead to under/overestimation of a given contribution. Generally, Fe^{III} -containing compounds have higher values of the f -factor than Fe^{II} -containing compounds thus the relative area of Fe^{III} site could be overestimated.^{43,44}

Synchrotron X-ray absorption spectroscopy (XAS) was performed at the Iron and Vanadium K-edge energies in transmission mode at the ROCK beamline of the SOLEIL synchrotron facility, France.⁴⁵ The incident energy was selected using a Si(111) quick-XAS monochromator

with an oscillation frequency of 2 Hz. Three ionization chambers filled with an appropriated mixture of gases were used as detectors. Pristine and *ex situ* samples were prepared as composite electrodes $\sim 8\text{mg}/\text{cm}^2$ pellets, containing active material/carbon black/PTFE in a mass ratio of 60/30/10 and placed between the first and the second ionization chambers. The energy calibration was done by measuring simultaneously Fe or V foils placed between the second and third ionization chambers. Reference materials ($\text{Na}_3\text{V}^{\text{III}}_2(\text{PO}_4)_3$, $\text{Na}_3\text{Fe}^{\text{III}}_2(\text{PO}_4)_3$, $\text{Fe}^{\text{II}}\text{C}_2\text{O}_4 \cdot 2\text{H}_2\text{O}$) were measured to assign the oxidation states of Iron and Vanadium species. Each XAS spectrum was resulting from an average over 10 minutes. Data were processed using the modules Athena and Artemis from the Demeter software package.⁴⁶ For the Fe K-edge, Fourier transforms of the k^2 -weighted EXAFS oscillations were carried out in the k -range of 2.6 - 10.8 \AA^{-1} . Fitting was performed with the R range of 1.0 - 2.1 \AA , $dR = 0$, and sine window. The radial distance (R_i), the Debye-Waller factor (σ_i^2) were refined while the coordination number (N) and attenuation factor (S_0^2) were fixed as 6 and 0.95, respectively, and the energy shift (E^0) was refined and fixed in the last step. The V K-edge EXAFS oscillations were refined in the same way but with slightly different window values: the k -range of 2.7 - 10.7 \AA^{-1} , the R range of 1.0 - 2.2 \AA , $dR = 0$, sine window, the coordination number (N) of 6 and attenuation factor (S_0^2) of 0.7.

DSC measurements were recorded on a DSC204 F1 from Netzsch in aluminum crucibles with a 50 mL /min argon flow with a scan range of 298 - 573 K at a heating and cooling rate of 10 K /min.

Results and Discussion

Characterization of $\text{Na}_4\text{FeV}(\text{PO}_4)_3$ obtained through direct syntheses: Several routes were attempted in order to obtain the $\text{Na}_4\text{FeV}(\text{PO}_4)_3$ target material from direct synthesis. For each of them, parameters such as the nature of the precursors, the annealing temperature and dwell time were investigated, but did not lead to significant differences with the results we report here. Three samples are compared: the first one was obtained by the classical solid-state method with annealing of a stoichiometric ball-milled mixture of precursors at 700 °C in

Ar, and the two others were obtained by a sol-gel reaction followed by annealing at 700 °C in Ar/H₂ or in Ar. The XRD patterns of these three samples are compared in Figure 1a, and the corresponding unit cell parameters are listed in Table 1 (see also Figures S1-S3 for more information on the Le Bail refinements of the XRD data).

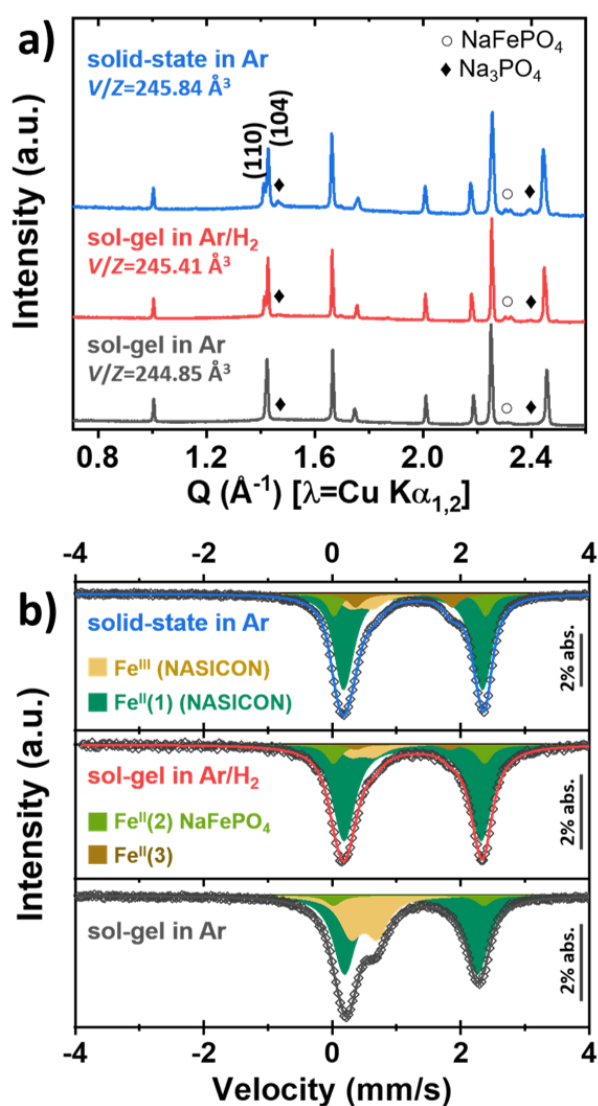


Figure 1. (a) X-ray diffraction patterns of the target composition $\text{Na}_4\text{FeV}(\text{PO}_4)_3$ obtained through various synthesis conditions. (\diamond) and (\circ) signs indicate Na_3PO_4 and NaFePO_4 as impurities, respectively. (b) Room temperature ^{57}Fe Mössbauer spectra of the corresponding samples. Each spectrum is described by the sum of different signals: Fe^{III} (light brown), $\text{Fe}^{\text{II}}(1)$ (dark green), $\text{Fe}^{\text{II}}(2)$ in NaFePO_4 (light green), and $\text{Fe}^{\text{II}}(3)$ (dark brown). Details of the refined parameters are listed in Table S1.

The sample obtained by solid state reaction in Ar shows the largest V/Z value (245.84(2) Å³), indicative of a larger number of Na⁺ incorporated into the NASICON structure (and hence higher Fe^{II} content) according to the chemical formula Na_{3+x}Fe^{II}_xFe^{III}_{1-x}V^{III}₁(PO₄)₃. However, when more Fe^{II} (thus more Na⁺) was evidenced in the obtained NASICON, higher amounts of impurities such as NaFePO₄ (◆) and Na₃PO₄ (○) were found, suggesting the formation of a compound not belonging to the solid solution Na_{3+x}Fe^{II}_xFe^{III}_{1-x}V^{III}₁(PO₄)₃ (with no longer a molar ratio Fe:V of 1:1). Earlier work on the Fe/V-mixed system³⁴ also reported that the NaFePO₄ impurity was formed when $x > 0.5$ in Na_{3+x}Fe^{II}_xV^{III}_{2-x}(PO₄)₃. Although we tried a large panel of synthesis routes and conditions, we never succeeded to fully reduce Fe into Fe^{II} so as to form pure Na₄FeV(PO₄)₃ through direct synthesis methods.

Table 1. Unit cell parameters of the target composition Na₄FeV(PO₄)₃ obtained through various synthesis conditions.

Synthesis conditions	a (Å)	c (Å)	c/a	V (Å ³)	V/Z (Å ³)
Solid-state in Ar	8.9084(8)	21.4629(8)	2.409	1475.09(9)	245.84(2)
Sol-gel in Ar/H ₂	8.9003(3)	21.4634(8)	2.412	1472.46(3)	245.41(2)
Sol-gel in Ar	8.8672(3)	21.5745(9)	2.433	1469.09(3)	244.85(2)
Sol-gel in Ar [ref. 35]	8.8833(3)	21.5092(7)	2.421	1469.95(5)	244.99(2)

⁵⁷Fe Mössbauer spectroscopy experiments were undertaken to precisely determine the valence state and local environment of Fe in the resulting samples. The corresponding ⁵⁷Fe Mössbauer spectra measured at 298 K and refined hyperfine parameters are displayed in Figure 1b and Table S1, respectively. The three NASICON samples exhibit various Fe^{III}/Fe^{II} ratios as shown by the signals labelled Fe^{III} and Fe^{II}(1). The sample prepared via sol-gel reaction and annealed in Ar contains a much larger amount of Fe^{III} (31(3) % of total Fe) than for the two other samples. Only 13 % and 10 % of remaining Fe^{III} are observed in the NASICON phases in the samples synthesized by the solid-state reaction in Ar and by the sol-gel reaction followed by an annealing in Ar/H₂, respectively. These results are in rather good agreement with the conclusions already drawn from the XRD data, the two latter samples being much more reduced and thus richer in Na than the first one (sol-gel in Ar). The second contribution

attributed to Fe^{II}, labelled as Fe^{II}(2), corresponds to 5 % to 11 % of the total Fe amount and is due to the presence of NaFePO₄, identified by XRD to be present as an impurity in the three samples.^{47,48} The third contribution attributed to Fe^{II}, labelled as Fe^{II}(3), is discussed in supplementary information only as not identified yet.

Characterization of Na₄FeV(PO₄)₃ obtained from Na₃FeV(PO₄)₃ through electrochemical sodiation. A pure phase of Na₄FeV(PO₄)₃ was prepared by electrochemical sodiation from Na₃FeV(PO₄)₃. The XRD patterns of Na₃FeV(PO₄)₃ (sample A) and of the two samples obtained by electrochemical sodiation down to cut-off voltages of 2.0 V (sample B) and 1.3 V (sample C) vs. Na⁺/Na are presented in Figure 2a.

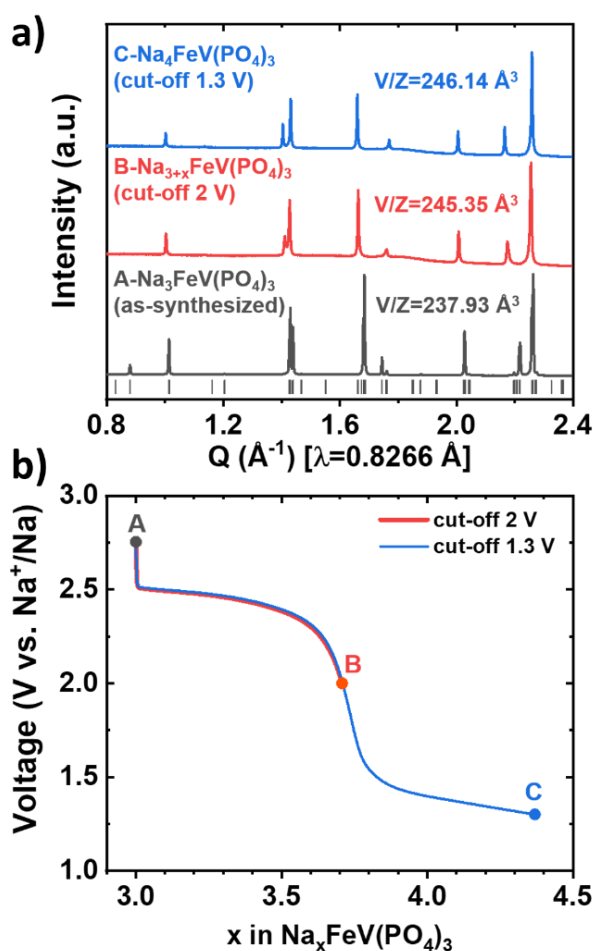


Figure 2. (a) X-ray diffraction patterns of pure Na₃FeV(PO₄)₃ (black) and of samples obtained electrochemically: “B” by electrochemical sodiation of Na₃FeV(PO₄)₃ at a cut-off voltage of 2 V (red), and “C” at a cut-off voltage of 1.3 V (blue). (b) The corresponding electrochemical data.

The presence of the extra (111) reflection peak at 0.9 \AA^{-1} in the XRD pattern of $\text{Na}_3\text{FeV}(\text{PO}_4)_3$ is a clear signature of a monoclinic distortion of the NASICON framework. When Na^+ is intercalated via electrochemical process, the monoclinic distortion disappears indicating the formation of $\text{Na}_4\text{FeV}(\text{PO}_4)_3$ to occur within rhombohedral symmetry. Note that the detailed descriptions of both structures will be presented later in this paper. Upon Na^+ intercalation into $\text{Na}_3\text{FeV}(\text{PO}_4)_3$, through a solid solution mechanism (paper to be submitted) the unit-cell volume (V/Z) gradually increases from 237.93 \AA^3 for $\text{Na}_3\text{FeV}(\text{PO}_4)_3$ to 245.35 \AA^3 for sample B, then to 246.14 \AA^3 for sample C. According to the electrochemical data presented in Figure 2b, the composition $\text{Na}_{3.7}\text{FeV}(\text{PO}_4)_3$ was predicted for sample B (cut-off voltage of 2 V). In literature, a typical lower cut-off voltage for Fe-based NASICON materials is set as 2.0 V vs. Na^+/Na but the $\text{Fe}^{\text{III/II}}$ redox couple is often partially activated.^{28,30,34-36} More Na^+ cations could be further intercalated by setting the lower cut-off voltage to 1.3 V vs. Na^+/Na , which yielded to the composition $\text{Na}_4\text{FeV}(\text{PO}_4)_3$, concomitant with the reaction at $\sim 1.5 \text{ V}$ being likely attributed to the reaction of carbon black or electrolyte decomposition as reported for the electrochemical synthesis of $\text{Na}_4\text{Ti}_2(\text{PO}_4)_3$ from $\text{Na}_3\text{Ti}_2(\text{PO}_4)_3$.²⁰ The large voltage difference between the two compositions was observed and this sluggish sodiation process could be due to big agglomerates in the sample (Figure S7). Figure S8 shows the electrochemical curve obtained from a battery cell containing only carbon black clearly suggesting that the second domain (below 1.5 V) is not attributed to the active material. Based on this observation, the second domain is mainly due to side reactions with carbon but contribution of side reactions from electrolyte cannot be excluded. The electrochemically-obtained, pure $\text{Na}_4\text{FeV}(\text{PO}_4)_3$ (i.e. without any trace of NaFePO_4 or Na_3PO_4) shows a significantly bigger unit-cell volume than that obtained from direct syntheses.

To further characterize the oxidation states and local environments of vanadium and iron in $\text{Na}_3\text{FeV}(\text{PO}_4)_3$ and electrochemically-sodiated $\text{Na}_4\text{FeV}(\text{PO}_4)_3$, synchrotron X-ray absorption spectroscopy experiments were conducted, including X-ray absorption near-edge structure (XANES) and extended X-ray absorption fine structure (EXAFS) at the Fe and V K-edges. The Fe and V K-edge X-ray absorption near-edge structure (XANES) spectra are reported in Fig 3a and 3b respectively. The edge position of $\text{Na}_3\text{Fe}^{\text{III}}\text{V}(\text{PO}_4)_3$ shifts towards lower energy upon Na^+ intercalation, indicating a complete reduction of Fe^{III} to Fe^{II} in sample C (Figure 3a), while

only a partial reduction of Fe is observed in sample B. The low intensities of the Fe pre-edge features indicate centrosymmetric octahedral environments for both high-spin Fe^{II} and Fe^{III} (inset of Figure 3a), as predicted for regular MO₆ octahedra.^{49,50} Concerning the XANES spectra at V K-edge, the edge positions of the three samples remained unchanged confirming that vanadium maintains its V^{III} oxidation state upon Na⁺ insertion. In particular, the reaction taking place at around 1.5 V Na⁺/Na does not involve the V^{III/II} redox couple with the reduction of V^{III} into V^{II}, most likely because four Na⁺ ions (as maximum) have already been incorporated in the NASICON structure. Furthermore, the vanadium pre-edge energies and intensities are preserved, confirming the V^{III}O₆ regular coordination. The more intense pre-peak at ~5470 eV is related to a lower V-V coordination compared to that in the Na₃V₂(PO₄)₃ reference compound (inset of Figure 3b).

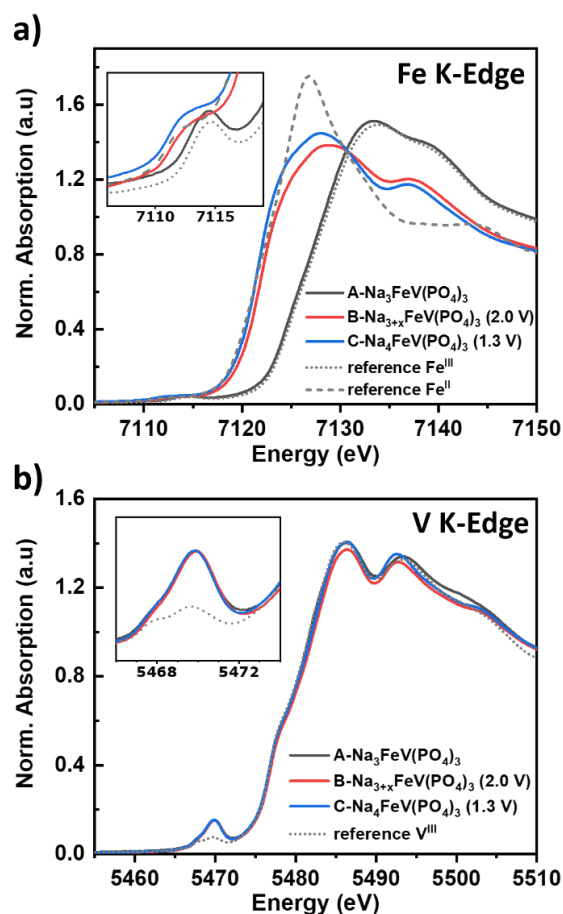


Figure 3. X-ray absorption spectroscopy data for pure Na₃FeV(PO₄)₃ (black) and electrochemically-sodiated samples at cut-off voltages of 2 V (red) and 1.3 V (blue). References for Fe and V K-edge XAS spectra: Fe^{III} (Na₃Fe₂(PO₄)₃), Fe^{II} (FeC₂O₄·2H₂O), V^{III} (Na₃V₂(PO₄)₃). See supporting information for the corresponding EXAFS analysis.

The analysis of the Extended X-Ray Absorption Fine Structure (EXAFS) oscillations extracted at both Fe and V K-edges was performed to distinguish the local environment of FeO_6 and VO_6 octahedra in $\text{Na}_3\text{FeV}(\text{PO}_4)_3$ and in the newly obtained $\text{Na}_4\text{FeV}(\text{PO}_4)_3$. As the presence of regular FeO_6 and VO_6 octahedra was already inferred by the XANES data, a single Fe – O or V – O scattering path (i.e. 6 equal M-O distances in MO_6) is sufficient to refine the corresponding EXAFS oscillations in the R range 1-2 Å. The obtained structural parameters are summarized in Tables S2 and S3. We found that the average Fe – O bond distance increases from 1.986(5) Å for the Fe^{III} -rich compound $\text{Na}_3\text{FeV}(\text{PO}_4)_3$ to 2.067(5) Å for the Fe^{II} -rich compound $\text{Na}_4\text{FeV}(\text{PO}_4)_3$, while that of V – O remains almost unchanged (2.018(5) - 2.023(5) Å) as expected for these two V^{III} -rich compounds. $\text{Na}_3\text{Fe}_2(\text{PO}_4)_3$ and $\text{Na}_3\text{V}_2(\text{PO}_4)_3$ were used as references for Fe^{III} and V^{III} with average Fe – O and V – O distances equal to 1.986(5) and 2.018(5) Å, respectively, in good agreement with those determined for $\text{Na}_3\text{FeV}(\text{PO}_4)_3$ as well as with those reported in literature for V – O.⁵¹

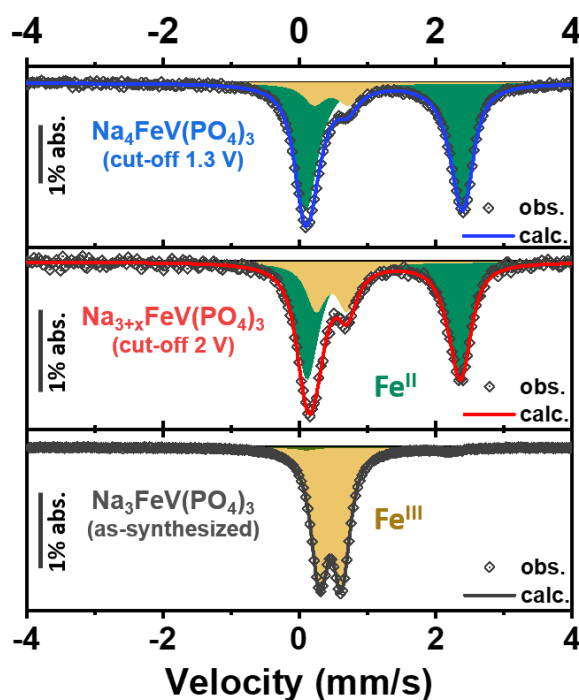


Figure 4. Room temperature ^{57}Fe Mössbauer spectra collected for $\text{Na}_3\text{FeV}(\text{PO}_4)_3$ and for the samples electrochemically sodiated at cut-off voltages of 2 V and 1.3 V. Each spectrum is described by the sum of two quadrupole doublets associated with Fe^{III} (light brown) and Fe^{II} (dark green). The corresponding refined hyperfine parameters are reported in Table S4.

The ^{57}Fe Mössbauer spectra collected for $\text{Na}_3\text{FeV}(\text{PO}_4)_3$ (sample A) and for the two samples obtained by electrochemical sodiation (sample B and C) are displayed in Figure 4 and the corresponding refined Mössbauer parameters are listed in Table S4. The spectrum of $\text{Na}_3\text{FeV}(\text{PO}_4)_3$ supports the successful synthesis of a pure phase, the quadrupole doublet accounting for 97(3) % of the total Fe amount, despite a very tiny contribution (3(3) %) associated with a partial reduction of Fe^{III} into Fe^{II} . The Mössbauer parameters describing the main signal are typical of high-spin Fe^{III} in an octahedral environment with oxygen surrounding.^{52, 53} The Mössbauer spectra of electrochemically sodiated samples clearly show the reduction of Fe^{III} to Fe^{II} without any impurity signal. The spectrum of $\text{Na}_4\text{FeV}(\text{PO}_4)_3$ (sample C) indicates the main doublet associated with Fe^{II} corresponding to at least 87(3) % of the total Fe amount. A trace of Fe^{III} signal was observed in the Mössbauer spectrum, which is not the case for XAS data probably because long acquisition (over 72 hours) for the Mössbauer spectroscopy may cause a slight oxidation of Fe^{II} . Full determination of the composition and structure of $\text{Na}_3\text{FeV}(\text{PO}_4)_3$ and $\text{Na}_4\text{FeV}(\text{PO}_4)_3$ is given in the following, based on XRD data.

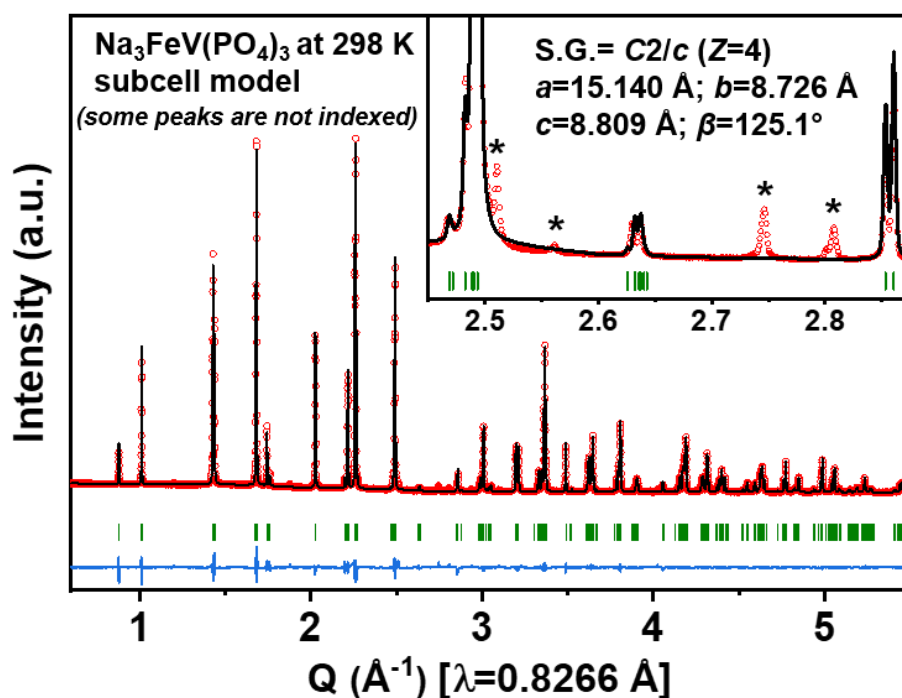


Figure 5. Le Bail analysis of $\text{Na}_3\text{FeV}(\text{PO}_4)_3$ XRD pattern with the subcell model reported in the literature [ref 30]. Asterisk marks refer to the unindexed superstructure reflections.

Crystal structure determination of $\text{Na}_3\text{FeV}(\text{PO}_4)_3$ and $\text{Na}_4\text{FeV}(\text{PO}_4)_3$: A structural model reported in the literature for $\text{Na}_3\text{FeV}(\text{PO}_4)_3$ ³⁰ was used as a starting point to describe the crystal structure of the $\text{Na}_3\text{FeV}(\text{PO}_4)_3$ sample obtained in this study : space group $C2/c$ ($Z = 4$) with $a = 15.140(2)$ Å, $b = 8.726(2)$ Å, $c = 8.809(2)$ Å, $\beta = 125.1(2)^\circ$, and $V/Z = 238.0(2)$ Å³. As shown in Figure 5 the subcell model allows to index the main reflections but, as highlighted with asterisks in the Q-range of 2.5 - 2.85 Å⁻¹ (inset of Figure 5), few of them remain unindexed and would correspond to superstructure reflections. Thermal analyses combining DSC and *in situ* temperature XRD were performed to confirm the existence of possible order-disorder phase transitions depending on the temperature, as already observed for the two end members of the solid solution $\text{Na}_3\text{Fe}_{2-x}\text{V}_x(\text{PO}_4)_3$ ($\text{Na}_3\text{Fe}_2(\text{PO}_4)_3$ ^{10,11} and $\text{Na}_3\text{V}_2(\text{PO}_4)_3$ ^{9,54}), as illustrated in Figure 6.

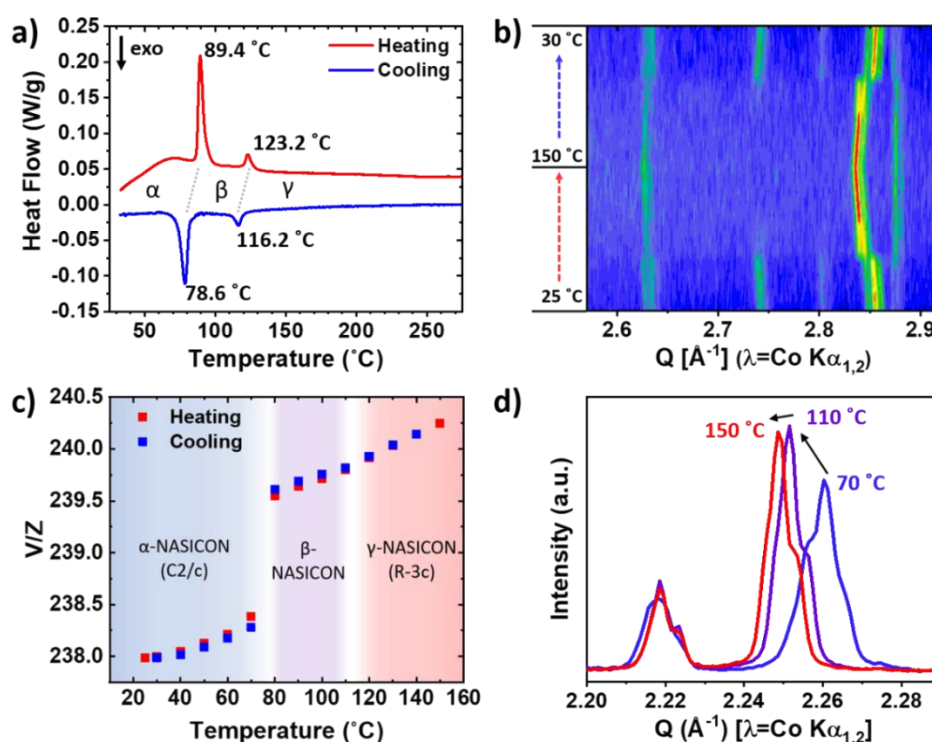


Figure 6. (a) DSC measurements of $\text{Na}_3\text{FeV}(\text{PO}_4)_3$ between 25 and 275 °C, upon heating and upon cooling. (b) XRD patterns collected *in situ* for $\text{Na}_3\text{FeV}(\text{PO}_4)_3$ every 10 °C upon heating up to 150 °C and then upon cooling down to 30 °C. (c) The corresponding V/Z evolution as a function of the temperature. (d) Selected *in situ* temperature XRD patterns collected before and after the phase transitions (70, 110, and 150 °C). The XRD patterns of the intermediate β phase were refined using $R-3c$ space group for comparison purpose.

According to DSC data (Figure 6a), two reversible phase transitions are indeed observed for $\text{Na}_3\text{FeV}(\text{PO}_4)_3$ at around 89.4 °C and 123.2 °C during heating, the specific heat capacity of the first phase transition (4.0 J/g) being much higher than that of the second one (0.7 J/g). *In situ* temperature XRD measurements further confirm the order-disorder phase transitions. Indeed, as clearly seen in Figure 6b the superstructure reflections observed for the ordered phase for instance at 2.74 Å⁻¹ and 2.80 Å⁻¹ completely disappear above 80 °C during heating (until 150 °C), and reversibly appear again upon cooling back to 30 °C. No detailed structural study of the intermediate β phase was reported yet and therefore the XRD patterns were refined using the $R\text{-}3c$ space group for a comparison purpose. The V/Z evolutions observed as a function of the temperature (Figure 6c) show that a significant cell volume change occurs during the first phase transition ($\alpha \leftrightarrow \beta$), whereas only progressive cell volume changes are observed during the second phase transition ($\beta \leftrightarrow \gamma$). A zoomed view of the XRD patterns corresponding to the three identified forms of $\text{Na}_3\text{FeV}(\text{PO}_4)_3$ (α , β and γ) is shown in Figure 6d. It is very likely that the crystal structures of the β and γ phases are indeed very closely related and only subtle site occupancy changes of the Na sites are expected to occur.

We determined the crystal structure of $\text{Na}_3\text{FeV}(\text{PO}_4)_3$ from Rietveld refinement using high-angular resolution synchrotron XRD powder pattern and considering a unit cell tripled along c-axis compared to that proposed by Zhou et al.³⁰ The result of Rietveld refinement is illustrated in Figure 7a and the corresponding structural parameters are listed in Table 2. $\text{Na}_3\text{FeV}(\text{PO}_4)_3$ crystallizes in a monoclinic cell (space group $C2/c$, $Z = 12$) with the lattice parameters of $a = 15.1394(2)$ Å; $b = 8.72550(12)$ Å; $c = 21.6142(3)$ Å; $\beta = 90.1744(9)^\circ$, and $V/Z = 237.932(6)$ Å³. It is noteworthy that this model can fully explain the reflections which were not indexed with the sub-cell model (inset of Figure 7a compared to inset of Figure 5). Similar unit cells have been reported for the structures of the two end members, $\alpha\text{-Na}_3\text{Fe}_2(\text{PO}_4)_3$ ^{10,11,13} measured at 298 K and for $\alpha\text{-Na}_3\text{V}_2(\text{PO}_4)_3$ ⁹ at 263 K, and thus we can conclude that the α form of $\text{Na}_3\text{FeV}(\text{PO}_4)_3$ is isostructural with the two end members.

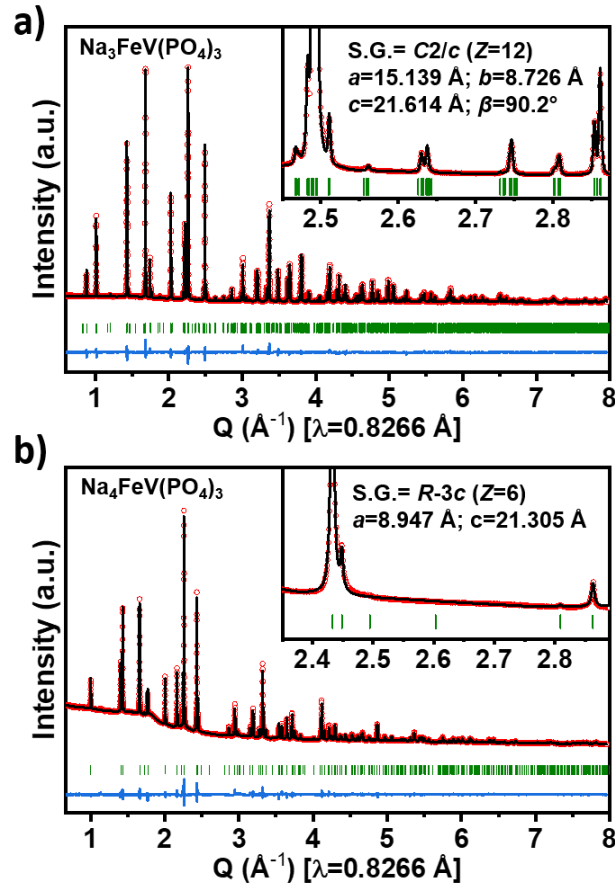


Figure 7. Rietveld refinement of (a) $\text{Na}_3\text{FeV}(\text{PO}_4)_3$ and (b) $\text{Na}_4\text{FeV}(\text{PO}_4)_3$.

Table 2. Refined structural parameters of $\text{Na}_3\text{FeV}(\text{PO}_4)_3$ at 298 K. The approximated coordinates of the vacancies are obtained from group-subgroup relation using the POWDER CELL software.⁵⁵ To find the coordinates, initially $R\text{-}3c$ space group unit cell was introduced and transformed to $P\text{-}3c$ (IIa, $a_{P\text{-}3c}=a_{R\text{-}3c}$, $b_{P\text{-}3c}=b_{R\text{-}3c}$, $c_{P\text{-}3c}=c_{R\text{-}3c}$) then $C2/c$ (I, $a_{C2/c}=a_{P\text{-}3c}-b_{P\text{-}3c}$, $b_{C2/c}=a_{P\text{-}3c}+b_{P\text{-}3c}$, $c_{C2/c}=c_{P\text{-}3c}$). Due to the cell transformation, Na(1) and Na(2) sites in the $R\text{-}3c$ space group split into two Na(1), and five Na(2) sites (containing two vacancies) in the $C2/c$ space group, respectively.

$\text{Na}_3\text{FeV}(\text{PO}_4)_3$

Space group: $C2/c$ (#15), $Z=12$

$a = 15.1394(2) \text{ \AA}$; $b = 8.72550(12) \text{ \AA}$; $c = 21.6142(3) \text{ \AA}$; $\beta = 90.1744(9)^\circ$

$V = 2855.19(8) \text{ \AA}^3$; $V/Z = 237.932(6) \text{ \AA}^3$

$R_{\text{wp}} = 4.36 \%$; $R_p = 2.87 \%$; $R_{\text{bragg}} = 5.50 \%$

Atom	Wyckoff	x/a	y/b	z/c	Uiso, \AA^2	Occ.
Fe/V(1a)	8f	0.0015(8)	-0.0004(13)	0.3532(7)	0.0078(9)	0.5/0.5
Fe/V(1b)	8f	0.3340(10)	0.0015(14)	0.3146(7)	0.0078(9)	0.5/0.5

Fe/V(1c)	8f	0.3336(9)	0.0023(13)	0.0190(7)	0.0078(9)	0.5/0.5
P(1a)	8f	0.1855(16)	0.147(3)	0.4179(9)	0.0081(8)	1
P(1b)	4e	0	0.296(4)	0.25	0.0081(8)	1
P(1c)	8f	0.3526(4)	0.3591(5)	0.2525(2)	0.0081(8)	1
P(1d)	8f	0.5206(14)	0.148(3)	0.0804(9)	0.0081(8)	1
P(1e)	8f	0.1682(17)	0.210(2)	0.0879(9)	0.0081(8)	1
Na(1a)	4a	0	0	0	0.024(10)	1
Na(1b)	8f	0.347(2)	0.055(2)	0.1662(15)	0.024(10)	1
Na(2a)	8f	0.1838(19)	0.188(3)	0.2599(10)	0.024(10)	1
Na(2b)	8f	0.014(2)	0.320(4)	0.4138(12)	0.024(10)	1
Na(2c)	8f	0.169(3)	0.136(3)	0.5872(15)	0.024(10)	1
Vacancy(1)	8f	0.337	0.307	0.083	-	0
Vacancy(2)	4e	0	0.307	0.75	-	0
O(1a)	8f	0.261(3)	0.432(6)	0.246(2)	0.0056(12)	1
O(1b)	8f	0.249(2)	0.106(5)	0.079(2)	0.0056(12)	1
O(1c)	8f	0.084(2)	0.396(5)	0.243(2)	0.0056(12)	1
O(1d)	8f	0.341(3)	0.185(3)	0.258(2)	0.0056(12)	1
O(1e)	8f	0.429(2)	0.076(5)	0.079(2)	0.0056(12)	1
O(1f)	8f	0.084(3)	0.112(5)	0.084(2)	0.0056(12)	1
O(1g)	8f	0.093(2)	0.074(5)	0.414(2)	0.0056(12)	1
O(1h)	8f	0.510(3)	0.321(3)	0.088(2)	0.0056(12)	1
O(1i)	8f	0.176(3)	0.321(3)	0.4172(19)	0.0056(12)	1
O(2a)	8f	0.245(3)	0.107(5)	0.3626(16)	0.0056(12)	1
O(2b)	8f	0.572(3)	0.134(5)	0.0190(14)	0.0056(12)	1
O(2c)	8f	0.403(3)	0.396(5)	0.1939(14)	0.0056(12)	1
O(2d)	8f	0.002(2)	0.206(5)	0.3104(14)	0.0056(12)	1
O(2e)	8f	0.153(2)	0.327(4)	0.0375(13)	0.0056(12)	1
O(2f)	8f	0.189(2)	0.292(4)	0.1495(13)	0.0056(12)	1
O(2g)	8f	0.393(3)	0.429(5)	0.3108(15)	0.0056(12)	1
O(2h)	8f	0.231(3)	0.091(4)	0.4774(15)	0.0056(12)	1
O(2i)	8f	0.571(2)	0.070(5)	0.1320(14)	0.0056(12)	1

The new $\text{Na}_4\text{FeV}(\text{PO}_4)_3$ composition crystallizes in the rhombohedral space group $R\text{-}3c$ with $a = 8.94656(8) \text{ \AA}$, $c = 21.3054(3) \text{ \AA}$, and $V/Z = 246.140(4) \text{ \AA}^3$ ($Z = 6$). Similar unit cell parameters are observed for $\text{Na}_4\text{Fe}_2(\text{PO}_4)_3$ ⁵⁶ ($a = 8.9543(9) \text{ \AA}$, $c = 21.280(4) \text{ \AA}$ and $V/Z = 246.26(7) \text{ \AA}^3$) and $\text{Na}_4\text{V}_2(\text{PO}_4)_3$ ¹⁹ ($a = 8.94(1) \text{ \AA}$, $c = 21.36(2) \text{ \AA}$ and $V/Z = 246.3 \text{ \AA}^3$). Although the ionic radii of Fe^{II} and V^{II} on one side and of Fe^{III} and V^{III} on the other side are

comparable (0.92 Å vs. 0.93 Å, and 0.785 Å vs. 0.78 Å, respectively), the a parameter decreases and the c parameter increases as Iron is replaced by Vanadium. The results of the structural refinement by the Rietveld method are illustrated in Figure 7b. As the unit cell volume of $\text{Na}_4\text{FeV}(\text{PO}_4)_3$ increases versus that of $\text{Na}_3\text{FeV}(\text{PO}_4)_3$ (+3.4 %) due to the intercalation of one additional Na^+ , most of the peaks shift towards lower angles and many reflections disappear since the transition from a monoclinic supercell to a rhombohedral cell increases the symmetry (inset of Figure 7b). The structural parameters are summarized in Table 3.

Table 3. Refined structural parameters of $\text{Na}_4\text{FeV}(\text{PO}_4)_3$ at 298 K.

$\text{Na}_4\text{FeV}(\text{PO}_4)_3$						
Space group: $R\text{-}3c$ (#167); $Z=6$						
$a = 8.94656(8)$ Å; $c = 21.3054(3)$ Å; $c/a = 2.381$						
$V = 1476.84(3)$ Å ³ ; $V/Z = 246.140(4)$ Å ³						
$R_{\text{wp}} = 12.5$ %; $R_{\text{p}} = 15.1$ %; $R_{\text{bragg}} = 5.03$ %						
Atom	Wyckoff	x/a	y/b	z/c	Uiso, Å²	Occ.
Fe/V(1)	12c	0	0	0.1483(3)	0.0066(3)	0.5/0.5
P(1)	18e	0.2967(5)	0	0.25	0.0115(5)	1
Na(1)	6b	0	0	0	0.0203(15)	0.958(5)
Na(2)	18e	0.6414(9)	0	0.25	0.0224(13)	0.958(8)
O(1)	36f	0.0134(9)	0.2064(9)	0.1921(4)	0.0166(9)	1
O(2)	36f	0.1858(6)	0.1701(9)	0.0848(5)	0.0136(8)	1

Figure 8 gives a schematic representation of the “lantern” units with adjacent Na^+ ions in $\text{Na}_3\text{FeV}(\text{PO}_4)_3$ and $\text{Na}_4\text{FeV}(\text{PO}_4)_3$. For $\text{Na}_3\text{FeV}(\text{PO}_4)_3$, two types of lanterns are observed due to Na^+ ordering and thus to different Na^+ distributions around both of them. On the contrary a single environment is observed in $\text{Na}_4\text{FeV}(\text{PO}_4)_3$ as the Na sites are fully occupied. Indeed, only 6 atomic positions are necessary to describe the structure of $\text{Na}_4\text{FeV}(\text{PO}_4)_3$ whereas 31

independent atomic positions are required to fully describe that of $\text{Na}_3\text{FeV}(\text{PO}_4)_3$ because of the symmetry reduction. In $\text{Na}_3\text{FeV}(\text{PO}_4)_3$, the Na(1) site (6-fold coordination, $6b$) in the rhombohedral form splits into Na(1a) and Na(1b) sites while the Na(2) site splits into five different ones: the fully occupied Na(2a), Na(2b), and Na(2c) sites and two emptied sites ($4e$ and $8f$ Wyckoff positions, see Table 2). Therefore, each Na(1a) or Na(1b) atom is surrounded by four occupied neighboring Na(2a), Na(2b) or Na(2c) positions and two Na^+ vacant sites in $\text{Na}_3\text{FeV}(\text{PO}_4)_3$ (Figure 8). In $\text{Na}_4\text{FeV}(\text{PO}_4)_3$, the two sodium sites Na(1) and Na(2) are almost fully occupied, with occupancy factors higher than 0.95. The composition, as determined from the analysis of the XRD data is thus $\text{Na}_{3.83(3)}\text{FeV}(\text{PO}_4)_3$. For comparison the occupancy factors of Na(1) and Na(2) sites in $\text{Na}_4\text{MnV}(\text{PO}_4)_3$ are 0.96 and 1.00, respectively³¹, or 0.949(9) and 0.904(4), respectively³².

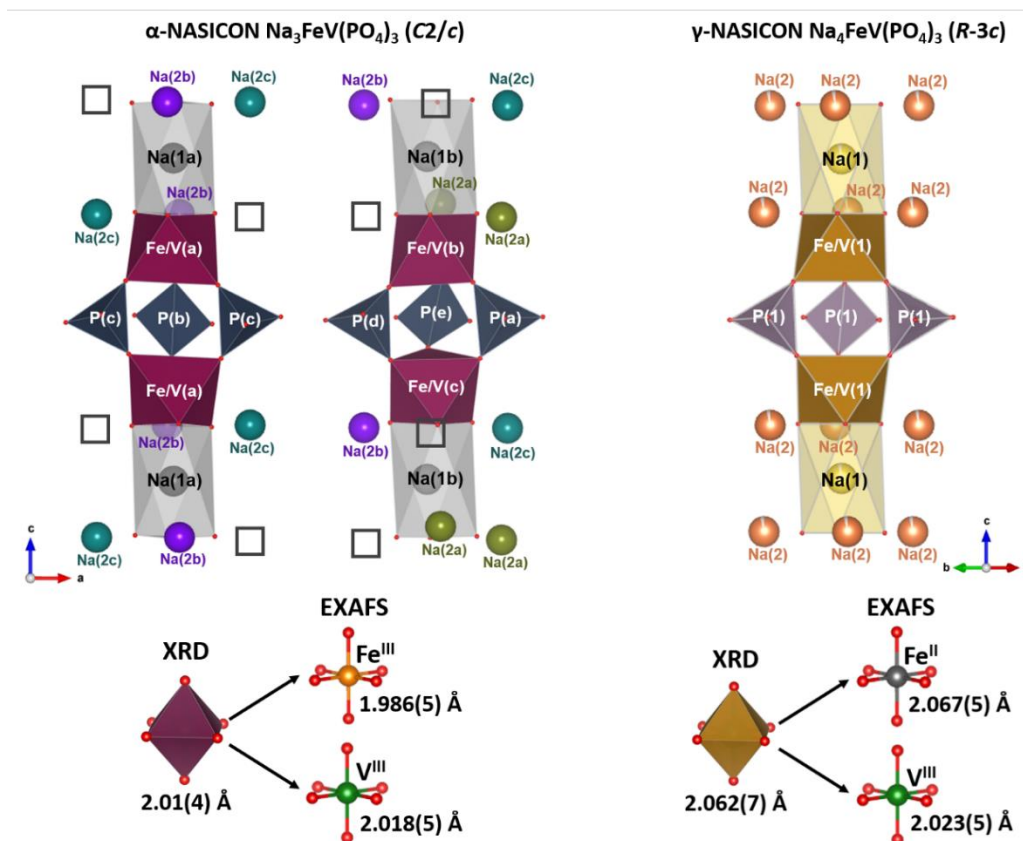


Figure 8. (top) Schematic representations of Na^+ distributions in $\text{Na}_3\text{FeV}(\text{PO}_4)_3$ and $\text{Na}_4\text{FeV}(\text{PO}_4)_3$. (bottom) Illustration of average and local environments in the first coordination shells obtained by XRD and EXAFS, respectively.

The selected interatomic distances determined in Na₃FeV(PO₄)₃ and Na₄FeV(PO₄)₃ are summarized with bond valence sum values and polyhedron distortion parameters in Table 4.

Table 4. Selected interatomic distances in Na₃FeV(PO₄)₃ and Na₄FeV(PO₄)₃ with the average interatomic distance (Avg.), the bond valence sum (BVS) and the polyhedral distortion (Δ). BVS is calculated from the Zachariasen formula, $V_i = \sum_j \exp\left(\frac{r_0 - r_{ij}}{0.37}\right)$, where r_0 characterizes a cation-anion pair.⁵⁷ Polyhedral distortion is calculated from $\Delta = \frac{1}{N} \sum_{i=1}^N \frac{(d_i - \bar{d})^2}{\bar{d}^2}$, where N is number of considered bond distances, d_i is the bond distance between central atom and oxygen, and \bar{d} is the average bond distance considered.

Na ₃ FeV(PO ₄) ₃ (C2/c)						Na ₄ FeV(PO ₄) ₃ (R-3c)					
Fe/V(1a)	O(1f)	2.12(4)	Fe/V(1b)	O(1a)	2.03(4)	Fe/V(1c)	O(1b)	2.04(4)	Fe/V(1)	O1	3 x 2.018(7)
	O(1g)	2.01(4)		O(1c)	1.99(4)		O(1e)	2.03(4)		O2	3 x 2.106(8)
	O(1h)	2.02(4)		O(1d)	2.02(3)		O(1i)	2.10(4)			
	O(2c)	1.99(4)		O(2a)	1.94(4)		O(2b)	2.04(4)			
	O(2d)	2.03(4)		O(2f)	2.01(4)		O(2e)	1.93(3)			
	O(2g)	1.97(4)		O(2i)	1.93(4)		O(2h)	1.97(4)			
Avg.		2.02(4)	Avg.		1.99(4)	Avg.		2.02(4)	Avg.		2.062(7)
BVS		2.96(4)	BVS		3.19(4)	BVS		2.93(4)	BVS		2.54(2)
Δ (x 10 ⁻⁴)		5.4	Δ (x 10 ⁻⁴)		3.8	Δ (x 10 ⁻⁴)		7.1	Δ (x 10 ⁻⁴)		3.9
Na(1a)	O(1f)	2 x 2.42(4)	Na(1b)	O(1a)	2.73(6)				Na(1)	O2	6 x 2.398(11)
	O(1g)	2 x 2.42(4)		O(1b)	2.44(5)						
	O(1h)	2 x 2.42(4)		O(1c)	2.62(6)						
				O(1d)	2.29(4)						
				O(1e)	2.28(5)						
				O(1i)	2.75(5)						
Avg.		2.43(5)	Avg.		2.52(5)				Avg.		2.398(11)
BVS		1.09(2)	BVS		1.00(2)				BVS		1.19(2)
Δ (x 10 ⁻⁴)		0.9	Δ (x 10 ⁻⁴)		59.2				Δ (x 10 ⁻⁴)		-
Na(2a)	O(1a)	2.44(5)	Na(2b)	O(1e)	2.40(5)	Na(2c)	O(1b)	2.43(5)	Na(2)	O1	2 x 2.950(11)
	O(1a)	2.40(5)		O(1f)	2.35(5)		O(1f)	2.51(5)		O1	2 x 2.565(9)
	O(1c)	2.39(5)		O(1g)	2.46(5)		O(1h)	2.43(6)		O2	2 x 2.509(10)
	O(1d)	2.39(5)		O(1i)	2.47(6)		O(1i)	2.37(6)		O2	2 x 2.490(8)
	O(2a)	2.50(4)		O(2b)	2.47(4)		O(2a)	2.82(5)			
	O(2d)	2.96(5)		O(2d)	2.45(4)		O(2b)	2.89(4)			
	O(2f)	2.56(4)		O(2e)	2.74(4)		O(2g)	2.46(4)			

	O(2g) 2.97(5)		O(2i) 2.71(4)		O(2h) 2.58(4)		
Avg.	2.58(5)	Avg.	2.51(5)	Avg.	2.56(5)	Avg.	2.628(10)
BVS	1.19(2)	BVS	1.27(2)	BVS	1.13(2)	BVS	0.95(2)
Δ ($\times 10^{-4}$)	100	Δ ($\times 10^{-4}$)	28.5	Δ ($\times 10^{-4}$)	48.3	Δ ($\times 10^{-4}$)	49.30

The average M – O (M = Fe, V) distance determined by XRD analysis increases from 2.01(4) Å in Na₃FeV(PO₄)₃ to 2.062(7) Å in Na₄FeV(PO₄)₃, leading thus to an increase of the MO₆ octahedra volume (+7.5 %) within the same order of magnitude than polyhedral distortion. However, the M – M distance within the lantern unit slightly decreases from 4.439(13) to 4.322(12) Å as well as the average Na(1) – O distance which decreases from 2.48(5) to 2.398(11) Å, leading thus to a significant decrease of the c parameter from 21.6142(3) Å to 21.3054(3) Å. The average Na(2) – O distance increases from 2.55(5) Å in Na₃FeV(PO₄)₃ to 2.628(10) Å in Na₄FeV(PO₄)₃. Bond valence sum (BVS) calculations result in an average value of 3.03(4) for Fe/V in Na₃Fe^{III}V^{III}(PO₄)₃ and of 2.54(2) in Na₄Fe^{II}V^{III}(PO₄) well consistent with both nominal chemical compositions. The BVS calculations also give reasonable values for Na in both compositions: 1.00(2) – 1.27(2) for Na₃FeV(PO₄)₃ and 0.95(2) – 1.19(2) for Na₃FeV(PO₄)₃ (see Table 4).

Table 5. Comparison of the unit cell volumes (V/Z) and the average M – O (M = Fe, V) distances obtained by X-ray diffraction and X-ray absorption (EXAFS) for Na_xFe₂(PO₄)₃, Na_xFeV(PO₄)₃ and Na_xV₂(PO₄)₃ (x = 3, 4).

Composition	X-ray Diffraction		X-ray Absorption		
	V/Z (Å ³)	Avg. Fe/V – O (Å)	Fe – O (Å)	V – O (Å)	Avg. Fe/V – O (Å)
Na₃Fe₂(PO₄)₃	237.1(2) ^[10]	2.004(13) ^[11]	1.986(5)	–	–
Na₃FeV(PO₄)₃	237.932(6)	2.01(4)	1.986(5)	2.018(5)	2.002(5)
Na₃V₂(PO₄)₃	237.786(2) ^[9]	2.003(5) ^[9]	–	2.018(5)	–
Na₄Fe₂(PO₄)₃	246.26(7) ^[56]	2.070(6) ^[56]	–	–	–
Na₄FeV(PO₄)₃	246.140(4)	2.062(7)	2.067(5)	2.023(5)	2.045(5)
Na₄V₂(PO₄)₃	246.3 ^[19]	–	–	–	–
	246.819(3)	2.071(18)	–	–	–

Furthermore, unit cell volumes (V/Z) and average $M-O$ ($M = Fe, V$) distances within $Na_3FeV(PO_4)_3$ and $Na_4FeV(PO_4)_3$, obtained by XRD and EXAFS analysis are compared with those of the two end members, $Na_xFe_2(PO_4)_3$ and $Na_xV_2(PO_4)_3$ ($x = 3$ and 4), in Table 5. $Na_3FeV(PO_4)_3$ shows cell volume and $M-O$ distances similar to the two end members: V/Z values of $237.1(2)^{10}$, $237.932(6)$, and $237.786(2)^9$ and $M-O$ distances of $2.004(13)^{11}$, $2.01(4)$, and $2.003(5)^9$ Å for $M = Fe, Fe/V$, and V in $Na_3M_2(PO_4)_3$, respectively. The three Na_4 -compounds also show similar values in cell volume and $M-O$ distances: V/Z values of $246.26(7)^{56}$, $246.140(4)$, and 246.3^{19} and $M-O$ distances of $2.070(6)^{56}$, $2.062(7)$, and $2.071(18)$ Å for $M = Fe, Fe/V$, and V in $Na_4M_2(PO_4)_3$, respectively. Overall, the average $M-O$ distances determined from XRD data are highly consistent with those determined from analysis of EXAFS data.

Electrochemical extraction of Na^+ from $Na_4FeV(PO_4)_3$. The electrochemically-sodiated $Na_4FeV(PO_4)_3$ electrode was cycled between 1.3 and 4.3 V vs. Na^+/Na at a C-rate of $C/20$ per Na^+ ion (Figure 9a). Upon the oxidation process, about 2.76 Na^+ ions are progressively extracted through the successive activations of the $Fe^{III/II}$, $V^{IV/III}$ and $V^{V/IV}$ redox couples, leading to a specific capacity of 153 mAh/g. In fact, the activation of the $V^{V/IV}$ redox couple above 3.9 V vs. Na^+/Na was also observed for other V-based $Na_xM_yV_{2-y}(PO_4)_3$ ($M = Al,^{19} Cr,^{27} Mn,^{31,32} Fe,^{34,35}$ and Mg^{38}) compounds. Furthermore, only two voltage domains are observed during discharge associated with the re-insertion of “only” 2.36 Na^+ ions, highlighting the asymmetry of the mechanisms involved upon charge and discharge. Apart from the asymmetric behavior, the electrochemical performance could be further optimized with a proper electrode engineering since the as-synthesized pristine powder of $Na_3FeV(PO_4)_3$ is a bare powder without carbon coating and characterized by rather big agglomerates ($> 20 \mu m$) (Figure S7). The two-domain behavior observed during discharge is quite different from the single solid solution behavior reported in $Na_4MnV(PO_4)_3$ between 2.5 – 4.3 V vs. Na^+/Na .³¹ On the one hand, $Na_4MnV(PO_4)_3$ shows an irreversible structural modification immediately occurs after the first charge and poor cyclability was observed, showing the capacity retention of about 40 % after 20 cycles.³¹ On the other hand, $Na_4FeV(PO_4)_3$ maintained its asymmetric mechanism during the next cycles and the capacity retention was almost doubled (ca. 78%)

after 20 cycles. Figure 9b presents the charge and discharge capacities of the electrochemically-sodiated $\text{Na}_4\text{FeV}(\text{PO}_4)_3$ electrode upon 20 cycles, showing the discharge capacities of the first and 20th cycles are 137.8 and 108.7 mAh/g, respectively. In order to clarify the origin of the electrochemical properties in this newly obtained pure $\text{Na}_4\text{FeV}(\text{PO}_4)_3$, in-depth structural and spectroscopic-related operando studies of the Na^+ extraction/insertion mechanism are currently in progress.

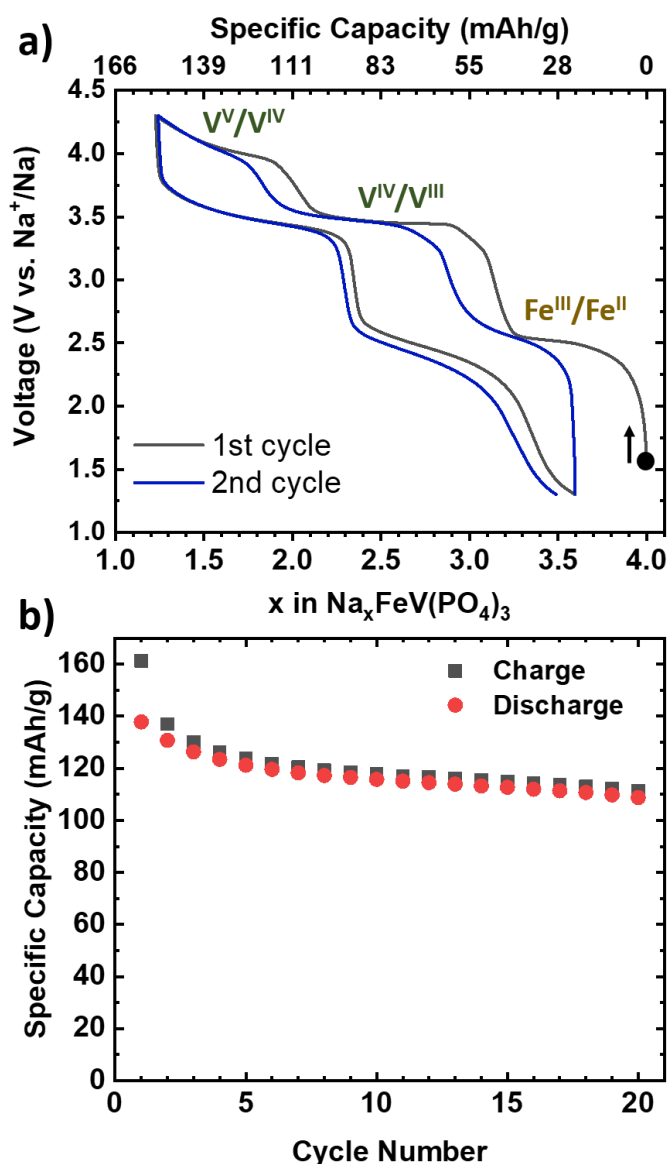


Figure 9. (a) Voltage-composition electrochemical profile of the electrochemically pre-sodiated $\text{Na}_4\text{FeV}(\text{PO}_4)_3$ during the first two cycles with a voltage window of 1.3 – 4.3 V vs. Na^+/Na at C/20 rate. **(b)** Associated charge and discharge capacities upon 20 cycles

Conclusion

We report for the first time on the rich crystal chemistry of the newly isolated $\text{Na}_4\text{FeV}(\text{PO}_4)_3$ composition as well as on the previously investigated $\text{Na}_3\text{FeV}(\text{PO}_4)_3$ for which we propose a new, more accurate model thanks to the analysis of high-angular resolution synchrotron X-ray diffraction data. This new structural model for $\text{Na}_3\text{FeV}(\text{PO}_4)_3$ at 298 K (α , $C2/c$, $Z=12$) can explain all the superstructure reflections due to long-range Na^+ ordering and is isostructural to the low-temperature form of $\text{Na}_3\text{M}_2(\text{PO}_4)_3$ ($M = \text{Fe}, \text{V}$). The observation of structural transitions ($\alpha \leftrightarrow \beta$ at 89 °C and $\beta \leftrightarrow \gamma$ at 123 °C) with and without the superstructure reflections further confirms the propensity of Na^+ order/disorder phenomena within NASICON materials. $\text{Na}_4\text{FeV}(\text{PO}_4)_3$ crystallizes in the $R-3c$ space group as other Na_4 -compounds reported in the literature, within which both Na(1) and Na(2) sites are almost fully occupied. Symmetric iron and vanadium local environments were found in both $\text{Na}_3\text{FeV}(\text{PO}_4)_3$ and $\text{Na}_4\text{FeV}(\text{PO}_4)_3$. Upon Na^+ intercalation into $\text{Na}_4\text{FeV}(\text{PO}_4)_3$, XANES and Mössbauer spectroscopies have shown the Fe reduction from (III) to (II) while the oxidation state of V remains (III). These results were also confirmed by EXAFS analysis, with the Fe – O bond length increasing from 1.986(5) Å to 2.067(5) Å while that of V – O remained almost unchanged and close to 2.02 Å. Therefore, we demonstrated that the substitution of V^{III} by Fe^{II} in $\text{Na}_4\text{FeV}(\text{PO}_4)_3$ allows more than two Na^+ exchange per two transition metals (about 2.36 Na^+) through $\text{Fe}^{\text{III/II}}$, $\text{V}^{\text{IV/III}}$ and $\text{V}^{\text{V/IV}}$ redox couples. Such a strategy can provide not only an increase in the specific capacity but also better sustainability.

Supporting Information

^{57}Fe Mössbauer refined parameters, powder patterns, EXAFS data, SEM images, and electrochemical curve of carbon electrode

Acknowledgements

The authors thank Cathy Denage and Emmanuel Petit (ICMCB) for technical support. The authors also acknowledge ALBA (Barcelona, Spain) for synchrotron X-ray diffraction experiments on the MSPD beamline (proposal number 20200024218) and SOLEIL (Gif-sur-Yvette, France) for X-ray spectroscopy experiments on the ROCK beamline (financed by the French National Research Agency (ANR) as a part of the “Investissements d’Avenir” program, reference ANR-10-EQPX-45; proposal number 20160282). The authors are grateful to the ANRT and TIAMAT for the funding (CIFRE grant) of SP’s PhD thesis. We acknowledge the financial support of Région Nouvelle Aquitaine and of the French National Research Agency (STORE-EX Labex Project ANR-10-LABX-76-01).

References

- (1) Zheng, Q.; Yi, H.; Li, X.; Zhang, H. Progress and Prospect for NASICON-Type $\text{Na}_3\text{V}_2(\text{PO}_4)_3$ for Electrochemical Energy Storage. *J. Energy Chem.* **2018**, *27* (6), 1597–1617. <https://doi.org/10.1016/j.jechem.2018.05.001>.
- (2) Zhang, X.; Rui, X.; Chen, D.; Tan, H.; Yang, D.; Huang, S.; Yu, Y. $\text{Na}_3\text{V}_2(\text{PO}_4)_3$: An Advanced Cathode for Sodium-Ion Batteries. *Nanoscale* **2019**, *11* (6), 2556–2576. <https://doi.org/10.1039/c8nr09391a>.
- (3) Hasa, I.; Mariyappan, S.; Saurel, D.; Adelhelm, P.; Kuposov, A. Y.; Masquelier, C.; Croguennec, L.; Casas-Cabanas, M. Challenges of Today for Na-Based Batteries of the Future: From Materials to Cell Metrics. *J. Power Sources* **2021**, *482*, 228872. <https://doi.org/10.1016/j.jpowsour.2020.228872>.
- (4) Li, H.; Wu, C.; Bai, Y.; Wu, F.; Wang, M. Controllable Synthesis of High-Rate and Long Cycle-Life $\text{Na}_3\text{V}_2(\text{PO}_4)_3$ for Sodium-Ion Batteries. *J. Power Sources* **2016**, *326*, 14–22. <https://doi.org/10.1016/j.jpowsour.2016.06.096>.
- (5) Yang, J.; Han, D. W.; Jo, M. R.; Song, K.; Kim, Y. Il; Chou, S. L.; Liu, H. K.; Kang, Y. M. $\text{Na}_3\text{V}_2(\text{PO}_4)_3$ Particles Partly Embedded in Carbon Nanofibers with Superb Kinetics for Ultra-High Power Sodium Ion Batteries. *J. Mater. Chem. A* **2015**, *3* (3), 1005–1009. <https://doi.org/10.1039/c4ta06001f>.
- (6) Xu, Y.; Wei, Q.; Xu, C.; Li, Q.; An, Q.; Zhang, P.; Sheng, J.; Zhou, L.; Mai, L. Layer-by-Layer $\text{Na}_3\text{V}_2(\text{PO}_4)_3$ Embedded in Reduced Graphene Oxide as Superior Rate and Ultralong-Life Sodium-Ion Battery Cathode. *Adv. Energy Mater.* **2016**, *6*(14). <https://doi.org/10.1002/aenm.201600389>.
- (7) Saravanan, K.; Mason, C. W.; Rudola, A.; Wong, K. H.; Balaya, P. The First Report on Excellent Cycling Stability and Superior Rate Capability of $\text{Na}_3\text{V}_2(\text{PO}_4)_3$ for Sodium Ion Batteries. *Adv. Energy Mater.* **2013**, *3* (4), 444–450. <https://doi.org/10.1002/aenm.201200803>.
- (8) Masquelier, C.; Croguennec, L. Polyanionic (Phosphates, Silicates, Sulfates) Frameworks as Electrode Materials for Rechargeable Li (or Na) Batteries. *Chem. Rev.* **2013**, *113* (8), 6552–6591. <https://doi.org/10.1021/cr3001862>.
- (9) Chotard, J.-N.; Rouse, G.; David, R.; Mentré, O.; Courty, M.; Masquelier, C. Discovery of a Sodium-Ordered Form of $\text{Na}_3\text{V}_2(\text{PO}_4)_3$ below Ambient Temperature. *Chem. Mater.* **2015**, *27* (17), 5982–5987. <https://doi.org/10.1021/acs.chemmater.5b02092>.
- (10) d'Yvoire, F.; Pintard-Scrépel, M.; Bretey, E.; de la Rochère, M. Phase Transitions and Ionic Conduction in 3D Skeleton Phosphates $\text{A}_3\text{M}_2(\text{PO}_4)_3$: A = Li, Na, Ag, K; M = Cr, Fe. *Solid State Ionics* **1983**, *9–10* (PART 2), 851–857. [https://doi.org/10.1016/0167-2738\(83\)90101-7](https://doi.org/10.1016/0167-2738(83)90101-7).
- (11) Masquelier, C.; Wurm, C.; Rodríguez-Carvajal, J.; Gaubicher, J.; Nazar, L. A Powder Neutron Diffraction Investigation of the Two Rhombohedral NASICON Analogues: $\gamma\text{-Na}_3\text{Fe}_2(\text{PO}_4)_3$ and $\text{Li}_3\text{Fe}_2(\text{PO}_4)_3$. *Chem. Mater.* **2000**, *12* (2), 525–532. <https://doi.org/10.1021/cm991138n>.
- (12) Bih, H.; Bih, L.; Manoun, B.; Azdouz, M.; Benmokhtar, S.; Lazor, P. Raman Spectroscopic Study of the Phase Transitions Sequence in $\text{Li}_3\text{Fe}_2(\text{PO}_4)_3$ and $\text{Na}_3\text{Fe}_2(\text{PO}_4)_3$ at High Temperature. *J. Mol. Struct.* **2009**, *936* (1–3), 147–155. <https://doi.org/10.1016/j.molstruc.2009.07.035>.
- (13) Kabbour, H.; Coillot, D.; Colmont, M.; Masquelier, C.; Mentré, O. $\alpha\text{-Na}_3\text{M}_2(\text{PO}_4)_3$ (M = Ti, Fe): Absolute Cationic Ordering in NASICON-Type Phases. *J. Am. Chem. Soc.* **2011**, *133* (31), 11900–

11903. <https://doi.org/10.1021/ja204321y>.
- (14) Song, W.; Ji, X.; Wu, Z.; Zhu, Y.; Yang, Y.; Chen, J.; Jing, M.; Li, F.; Banks, C. E. First Exploration of Na-Ion Migration Pathways in the NASICON Structure $\text{Na}_3\text{V}_2(\text{PO}_4)_3$. *J. Mater. Chem. A* **2014**, *2* (15), 5358–5362. <https://doi.org/10.1039/c4ta00230j>.
- (15) Ishado, Y.; Inoishi, A.; Okada, S. Exploring Factors Limiting Three- Na^+ Extraction from $\text{Na}_3\text{V}_2(\text{PO}_4)_3$. *Electrochemistry* **2020**, *88* (5), 457–462. <https://doi.org/10.5796/electrochemistry.20-00080>.
- (16) Pal, S. K.; Thirupathi, R.; Chakrabarty, S.; Omar, S. Improving the Electrochemical Performance of $\text{Na}_3\text{V}_2(\text{PO}_4)_3$ Cathode in Na-Ion Batteries by Si-Doping. *ACS Appl. Energy Mater.* **2020**, *3* (12), 12054–12065. <https://doi.org/10.1021/acsaem.0c02188>.
- (17) Mirza, S.; Song, Z.; Zhang, H.; Hussain, A.; Zhang, H.; Li, X. A Simple Pre-Sodiation Strategy to Improve the Performance and Energy Density of Sodium Ion Batteries with $\text{Na}_4\text{V}_2(\text{PO}_4)_3$ as the Cathode Material. *J. Mater. Chem. A* **2020**, *8* (44), 23368–23375. <https://doi.org/10.1039/d0ta08186h>.
- (18) Yao, X.; Zhu, Z.; Li, Q.; Wang, X.; Xu, X.; Meng, J.; Ren, W.; Zhang, X.; Huang, Y.; Mai, L. 3.0 V High Energy Density Symmetric Sodium-Ion Battery: $\text{Na}_4\text{V}_2(\text{PO}_4)_3\|\text{Na}_3\text{V}_2(\text{PO}_4)_3$. *ACS Appl. Mater. Interfaces* **2018**, *10* (12). <https://doi.org/10.1021/acsaami.7b16901>.
- (19) Lalère, F.; Seznec, V.; Courty, M.; David, R.; Chotard, J. N.; Masquelier, C. Improving the Energy Density of $\text{Na}_3\text{V}_2(\text{PO}_4)_3$ -Based Positive Electrodes through V/Al Substitution. *J. Mater. Chem. A* **2015**, *3* (31), 16198–16205. <https://doi.org/10.1039/C5TA03528G>.
- (20) Senguttuvan, P.; Rousse, G.; Dompablo, M. E. A. De; Vezin, H.; Tarascon, J. Low Potential Sodium Insertion in NASICON-Type Structure through the Ti(III)/Ti(II) Redox Couple. *J. Am. Chem. Soc.* **2013**, *135* (10), 3897–3903. <https://doi.org/10.1021/ja311044t>.
- (21) Lalère, F.; Seznec, V.; Courty, M.; Chotard, J. N.; Masquelier, C. Coupled X-Ray Diffraction and Electrochemical Studies of the Mixed Ti/V-Containing NASICON: $\text{Na}_2\text{TiV}(\text{PO}_4)_3$. *J. Mater. Chem. A* **2018**, *6* (15), 6654–6659. <https://doi.org/10.1039/c7ta10689k>.
- (22) Kawai, K.; Asakura, D.; Nishimura, S.; Yamada, A. Stabilization of 4.5 V $\text{Cr}^{4+}/\text{Cr}^{3+}$ Redox Reaction in NASICON-Type $\text{Na}_3\text{Cr}_2(\text{PO}_4)_3$ by Ti Substitution. *Chem. Commun.* **2019**, *55* (91), 13717–13720. <https://doi.org/10.1039/c9cc04860j>.
- (23) Zhu, T.; Hu, P.; Wang, X.; Liu, Z.; Luo, W.; Owusu, K. A.; Cao, W.; Shi, C.; Li, J.; Zhou, L.; Mai, L. Realizing Three-Electron Redox Reactions in NASICON-Structured $\text{Na}_3\text{MnTi}(\text{PO}_4)_3$ for Sodium-Ion Batteries. *Adv. Energy Mater.* **2019**, 1803436. <https://doi.org/10.1002/aenm.201803436>.
- (24) Patoux, S.; Rousse, G.; Leriche, J. B.; Masquelier, C. Structural and Electrochemical Studies of Rhombohedral $\text{Na}_2\text{TiM}(\text{PO}_4)_3$ and $\text{Li}_{1.6}\text{Na}_{0.4}\text{TiM}(\text{PO}_4)_3$ (M = Fe, Cr) Phosphates. *Chem. Mater.* **2003**, *15* (10), 2084–2093. <https://doi.org/10.1021/cm020479p>.
- (25) Tillement, O.; Couturier, J. C.; Angenault, J.; Querton, M. Crystal Chemistry and Electrical Study of $\text{Na}_x\text{NbTi}(\text{PO}_4)_3$. *Solid State Ionics* **1991**, *48* (3–4), 249–255. [https://doi.org/10.1016/0167-2738\(91\)90039-E](https://doi.org/10.1016/0167-2738(91)90039-E).
- (26) Kawai, K.; Zhao, W.; Nishimura, S.; Yamada, A. High-Voltage $\text{Cr}^{4+}/\text{Cr}^{3+}$ Redox Couple in Polyanion Compounds. *ACS Appl. Energy Mater.* **2018**, *1*, 928–931. <https://doi.org/10.1021/acsaem.7b00105>.
- (27) Liu, R.; Xu, G.; Li, Q.; Zheng, S.; Zheng, G.; Gong, Z.; Li, Y.; Kruskop, E.; Fu, R.; Chen, Z.; Amine, K.; Yang, Y. Exploring Highly Reversible 1.5-Electron Reactions ($\text{V}^{3+}/\text{V}^{4+}/\text{V}^{5+}$) in $\text{Na}_3\text{VCr}(\text{PO}_4)_3$

- Cathode for Sodium-Ion Batteries . *ACS Appl. Mater. Interfaces* **2017**, *9* (50), 43632–43639. <https://doi.org/10.1021/acsami.7b13018>.
- (28) Walczak, K.; Gedziorowski, B.; Kulka, A.; Zajac, W.; Ziabka, M.; Idczak, R.; Tran, V. H.; Molenda, J. Exploring the Role of Manganese on Structural, Transport and Electrochemical Properties of NASICON- $\text{Na}_3\text{Fe}_{2-y}\text{Mn}_y(\text{PO}_4)_3$ —Cathode Materials for Na-Ion Batteries. *ACS Appl. Mater. Interfaces* **2019**, *11*, 43046–43055. <https://doi.org/10.1021/acsami.9b10184>.
- (29) Gao, H.; Seymour, I. D.; Xin, S.; Xue, L.; Henkelman, G.; Goodenough, J. B. $\text{Na}_3\text{MnZr}(\text{PO}_4)_3$: A High-Voltage Cathode for Sodium Batteries. *J. Am. Chem. Soc.* **2018**, *140*, 18192–18199. <https://doi.org/10.1021/jacs.8b11388>.
- (30) Zhou, W.; Xue, L.; Lü, X.; Gao, H.; Li, Y.; Xin, S.; Fu, G.; Cui, Z.; Zhu, Y.; Goodenough, J. B. $\text{Na}_x\text{M}(\text{PO}_4)_3$ (M = Mn, Fe, Ni) Structure and Properties for Sodium Extraction. *Nano Lett.* **2016**, *16* (12), 7836–7841. <https://doi.org/10.1021/acs.nanolett.6b04044>.
- (31) Chen, F.; Kovrugin, V. M.; David, R.; Mentré, O.; Fauth, F.; Chotard, J.-N.; Masquelier, C. A NASICON-Type Positive Electrode for Na Batteries with High Energy Density: $\text{Na}_4\text{MnV}(\text{PO}_4)_3$. *Small Methods* **2018**, 1800218. <https://doi.org/10.1002/smt.201800218>.
- (32) Zakharkin, M. V.; Drozhzhin, O. A.; Tereshchenko, I. V.; Chernyshov, D.; Abakumov, A. M.; Antipov, E. V.; Stevenson, K. J. Enhancing Na^+ Extraction Limit through High Voltage Activation of the NASICON-Type $\text{Na}_4\text{MnV}(\text{PO}_4)_3$ Cathode. *ACS Appl. Energy Mater.* **2018**, *1* (11), 5842–5846. <https://doi.org/10.1021/acsaem.8b01269>.
- (33) Wang, J.; Wang, Y.; Seo, D. H.; Shi, T.; Chen, S.; Tian, Y.; Kim, H.; Ceder, G. A High-Energy NASICON-Type Cathode Material for Na-Ion Batteries—Supporting. *Adv. Energy Mater.* **2020**, *10* (10). <https://doi.org/10.1002/aenm.201903968>.
- (34) de Boisse, B. M.; Ming, J.; Nishimura, S.; Yamada, A. Alkaline Excess Strategy to NASICON-Type Compounds towards Higher-Capacity Battery Electrodes. *J. Electrochem. Soc.* **2016**, *163* (7), A1469–A1473. <https://doi.org/10.1149/2.0041608jes>.
- (35) Hadouchi, M.; Yaqoob, N.; Kaghazchi, P.; Tang, M.; Liu, J.; Sang, P.; Fu, Y.; Huang, Y.; Ma, J. Fast Sodium Intercalation in $\text{Na}_{3.41}\text{Fe}_{0.59}\text{V}(\text{PO}_4)_3$: A Novel Sodium-Deficient NASICON Cathode for Sodium-Ion Batteries. *Energy Storage Mater.* **2021**, *35*, 192–202. <https://doi.org/10.1016/j.ensm.2020.11.010>.
- (36) Aragón, M. J.; Lavela, P.; Ortiz, G. F.; Tirado, J. L. Effect of Iron Substitution in the Electrochemical Performance of $\text{Na}_3\text{V}_2(\text{PO}_4)_3$ as Cathode for Na-Ion Batteries. *J. Electrochem. Soc.* **2015**, *162* (2), A3077–A3083. <https://doi.org/10.1149/2.0151502jes>.
- (37) Liu, Y.; Zhou, Y.; Zhang, J.; Xia, Y.; Chen, T.; Zhang, S. Monoclinic Phase $\text{Na}_3\text{Fe}_2(\text{PO}_4)_3$: Synthesis, Structure, and Electrochemical Performance as Cathode Material in Sodium-Ion Batteries. *ACS Sustain. Chem. Eng.* **2017**, *5* (2), 1306–1314. <https://doi.org/10.1021/acssuschemeng.6b01536>.
- (38) Inoishi, A.; Yoshioka, Y.; Zhao, L.; Kitajou, A.; Okada, S. Improvement in the Energy Density of $\text{Na}_3\text{V}_2(\text{PO}_4)_3$ by Mg Substitution. *ChemElectroChem* **2017**, *4* (11), 2755–2759. <https://doi.org/10.1002/celec.201700540>.
- (39) Singh, B.; Wang, Z.; Park, S.; Gautam, G. S.; Chotard, J. N.; Croguennec, L.; Carlier, D.; Cheetham, A. K.; Masquelier, C.; Canepa, P. A Chemical Map of NASICON Electrode Materials for Sodium-Ion Batteries. *J. Mater. Chem. A* **2021**, *9* (1), 281–292. <https://doi.org/10.1039/d0ta10688g>.

- (40) Fauth, F.; Peral, I.; Popescu, C.; Knapp, M. The new material Science Powder Diffraction beam line at ALBA Synchrotron. *Powder Diffr.* **2013**, *28*, S360–S370.
- (41) Rodríguez-Carvajal, J. Recent Advances in Magnetic Structure Determination by Neutron Powder Diffraction. *Phys. B Phys. Condens. Matter* **1993**, *192* (1–2), 55–69. [https://doi.org/10.1016/0921-4526\(93\)90108-I](https://doi.org/10.1016/0921-4526(93)90108-I).
- (42) Petříček, V.; Dušek, M.; Palatinus, L. Crystallographic Computing System JANA2006: General Features. *Zeitschrift für Krist.* **2014**, *229* (5), 345–352. <https://doi.org/10.1515/zkri-2014-1737>.
- (43) Liu, J.; Mysen, B.; Fei, Y.; Li, J. Recoil-Free Fractions of Iron in Aluminous Bridgmanite from Temperature-Dependent Mössbauer Spectra. *Am. Mineral.* **2015**, *100* (8–9), 1978–1984. <https://doi.org/10.2138/am-2015-5245>.
- (44) Aldon, L.; Perea, A.; Womes, M.; Ionica-Bousquet, C. M.; Jumas, J. C. Determination of the Lamb-Mössbauer Factors of LiFePO_4 and FePO_4 for Electrochemical in Situ and Operando Measurements in Li-Ion Batteries. *J. Solid State Chem.* **2010**, *183* (1), 218–222. <https://doi.org/10.1016/j.jssc.2009.10.022>.
- (45) Briois, V.; La Fontaine, C.; Belin, S.; Barthe, L.; Moreno, T.; Pinty, V.; Carcy, A.; Girardot, R.; Fonda, E. ROCK: The New Quick-EXAFS Beamline at SOLEIL. *J. Phys. Conf. Ser.* **2016**, *712* (1). <https://doi.org/10.1088/1742-6596/712/1/012149>.
- (46) Ravel, B.; Newville, M. ATHENA, ARTEMIS, HEPHAESTUS: Data Analysis for X-Ray Absorption Spectroscopy Using IFEFFIT. *J. Synchrotron Radiat.* **2005**, *12* (4), 537–541. <https://doi.org/10.1107/S0909049505012719>.
- (47) Seo, J. Y.; Choi, H.; Kim, C. S.; Lee, Y. B. Crystal Structure and Magnetic Properties of Sodium-Iron Phosphates $\text{NaFe}_{0.9}\text{Mn}_{0.1}\text{PO}_4$ Cathode Material. *J. Korean Phys. Soc.* **2018**, *73* (12), 1863–1866. <https://doi.org/10.3938/jkps.73.1863>.
- (48) Kosova, N. V.; Podugolnikov, V. R.; Devyatkina, E. T.; Slobodyuk, A. B. Structure and Electrochemistry of NaFePO_4 and $\text{Na}_2\text{FePO}_4\text{F}$ Cathode Materials Prepared via Mechanochemical Route. *Mater. Res. Bull.* **2014**, *60*, 849–857. <https://doi.org/10.1016/j.materresbull.2014.09.081>.
- (49) Shulman, G. R.; Yafet, Y.; Eisenberger, P.; Blumberg, W. E. Observations and Interpretation of X-Ray Absorption Edges in Iron Compounds and Proteins. *Proc. Natl. Acad. Sci. U. S. A.* **1976**, *73* (5), 1384–1388. <https://doi.org/10.1073/pnas.73.5.1384>.
- (50) Westre, T. E.; Kennepohl, P.; DeWitt, J. G.; Hedman, B.; Hodgson, K. O.; Solomon, E. I. A Multiplet Analysis of Fe K-Edge $1s \rightarrow 3d$ Pre-Edge Features of Iron Complexes. *J. Am. Chem. Soc.* **1997**, *119* (27), 6297–6314. <https://doi.org/10.1021/ja964352a>.
- (51) Hu, P.; Zou, Z.; Sun, X.; Wang, D.; Ma, J.; Kong, Q.; Xiao, D.; Gu, L.; Zhou, X.; Zhao, J.; Dong, S.; He, B.; Avdeev, M.; Shi, S.; Cui, G.; Chen, L. Uncovering the Potential of M1-Site-Activated NASICON Cathodes for Zn-Ion Batteries. **2020**, *1907526*, 1–9. <https://doi.org/10.1002/adma.201907526>.
- (52) Menil, F. Systematic Trends of the ^{57}Fe Mössbauer Isomer Shifts in (FeO_n) and (FeF_n) Polyhedra. Evidence of a New Correlation between the Isomer Shift and the Inductive Effect of the Competing Bond T-X ($\rightarrow \text{Fe}$) (Where X Is O or F and T Any Element with a Formal Positive Charge). *J. Phys. Chem. Solids* **1985**, *46*(7), 763–789. [https://doi.org/10.1016/0022-3697\(85\)90001-0](https://doi.org/10.1016/0022-3697(85)90001-0).
- (53) Idczak, R.; Tran, V. H.; Świątek-Tran, B.; Walczak, K.; Zajac, W.; Molenda, J. The Effects of Mn Substitution on the Structural and Magnetic Properties of the NASICON-Type $\text{Na}_3\text{Fe}_{2-x}\text{Mn}_x(\text{PO}_4)_3$ Solid Solution. *J. Magn. Magn. Mater.* **2019**, *491*, 1–11. <https://doi.org/10.1016/j.jmmm.2019.04.044>.

- 019.165602.
- (54) Gaubicher, J.; Wurm, C.; Goward, G.; Masquelier, C.; Nazar, L. Rhombohedral Form of $\text{Li}_3\text{V}_2(\text{PO}_4)_3$ as a Cathode in Li-Ion Batteries. *Chem. Mater.* **2000**, *12* (11), 3240–3242. <https://doi.org/10.1021/cm000345g>.
- (55) Kraus, W.; Nolze, G. POWDER CELL - A Program for the Representation and Manipulation of Crystal Structures and Calculation of the Resulting X-Ray Powder Patterns. *J. Appl. Crystallogr.* **1996**, *29* (3), 301–303. <https://doi.org/10.1107/S0021889895014920>.
- (56) Hatert, F. $\text{Na}_4\text{Fe}^{2+}\text{Fe}^{3+}(\text{PO}_4)_3$, A New Synthetic NASICON-Type Phosphate. *Acta Crystallogr. Sect. E Struct. Reports Online* **2009**, *65* (4), i30–i30. <https://doi.org/10.1107/s1600536809009210>.
- (57) Brown, I. D.; Altermatt, D. Bond-Valence Parameters Obtained from a Systematic Analysis of the Inorganic Crystal Structure Database. *Acta Cryst.* **1985**, B41, 244–247. <https://doi.org/10.1107/S0108768185002063>.

Table of Contents

